The Doctoral Thesis

Characterizing fluid dynamics of the structure of dragonfly wing in life environments

Yusuke Fujita

Graduate School of Integrated Sciences for Life, Hiroshima University

Contents

Publication List

(1) **Yusuke Fujita**, Hiraku Nishimori and Makoto Iima, "Dead-Water Region around Two-Dimensional Sand-Dune Models", *Journal of the Physical Society of Japan*, **89**, 063901 (2020).

(2) **Yusuke Fujita** and Makoto Iima, "Dynamic Lift Enhancement Mechanism of Dragonfly Wing Model by Vortex-Corrugation Interaction", *Physical Review Fluids*, **8**, 123101 (2023).

(3) **Yusuke Fujita** and Makoto Iima, "Aerodynamic Performance of Dragonfly Wing Model That Starts Impulsively: How Vortex Motion Works", *Journal of Fluid Science and Technology*, **18**, 1, JFST0013 (2023).

Chapter 1

General introduction

1.1 Evolutionary significance of insect in adapting to complex environments

Living organisms have been evolving, reproducing, and going extinct for billions of years since their creation. Organisms that fail to adapt to rapid environmental changes often end up on the brink of extinction. Thus, to avoid extinction, organisms must continue to adapt to complex environments or move to better environments. To make these possible, organisms have optimized their morphology and locomotor abilities through natural selection.

Insects are considered to be the first organisms to take to the air in the history of the Earth [1]. They were able to extend their range of movement and enable a variety of survival strategies by making full use of their wings and flying. Thus, they reproduced all over the world and evolved into a variety of forms.

This doctoral thesis focuses on a dragonfly. Dragonflies are present on all continents except Antarctica, where they have a long evolutionary history [2]. Some dragonflies migrate between continents and perform complex predatory flights. Therefore, dragonflies have an optimal morphology that enables them to adapt to environmental changes and carry out survival strategies.

The above assertion implies that the exploration of insect morphology, encompassing dragonflies, holds significance not just within the realm of biology but also within the context of engineering. Researchers can study insect morphology to inform the design and optimization of technology inspired by biology. This spans from efficient robotic engineering to innovative aerospace systems. In recent years, there has been a demand for the development of robots capable of adapting to complex environments. Therefore, learning from organisms thriving in intricate environments is exceptionally crucial.

However, faithfully reproducing complex environments and the morphology of living organisms is a challenging task. Additionally, when creating robots for specific purposes, a faithful reproduction of an organism's complete morphology may not be necessary. Therefore, research focused on extracting crucial elements from biological organisms and understanding their characteristics is equally important. This fundamental study offers valuable insights into the development of advanced engineering solutions that imitate prominent features observed in the morphological study of insects.

1.2 Understanding the fluid dynamics of insect flight

This section is based on Ref. [3].

1.2.1 Fluid characteristics of insect flight

The aerodynamic characteristics of flying vehicles and organisms show a considerable amount of variety. Among this variety, flow characteristics are explained by the Reynolds number (Re). The Reynolds number is the ratio of inertial forces to viscous forces. It is defined as $Re = \frac{d|\boldsymbol{U}|}{\nu}$, where ν is the kinematic viscosity, d is the characteristic length, and $|\boldsymbol{U}|$ is the flow speed. The Reynolds number based on the wing chord as characteristic length during forward flight ranges from $O(10^0)$ (e.g., thrips) to $O(10^6)$ (e.g., passenger planes) [4]. Therefore, there is a diversity of flight characteristics. Insects' flight characteristics that differ from those of airplanes could be applied to various technologies, including small flying robots and drones, particularly in the low-Reynolds number regime, $O\left(10^2\right) - O\left(10^4\right)$ [5, 6, 7, 8, 9].

1.2.2 Aerodynamic insights into flapping motion and unsteady lift in insect flight

This study aims to investigate the aerodynamic benefits of insect flight in the low-Reynolds number regime. Insect flight is characterized by a flapping motion, which is not present in conventional airplanes. When an insect flaps its wings, a vortex known as a leading-edge vortex (LEV) is generated above the wings [10]. The generation of LEV is important for insects, in particular, to generate lift by flapping their wings and to fly against gravity [4, 10, 11, 12, 13, 14, 15].

The flapping motion is an important but quite complex movement. Therefore, it is often separated into multiple motion elements, including translational and rotational motion. In addition, several additional techniques for enhancing unsteady lift in insects are documented, such as delayed (or absence of) stall, wake capture, and the clap-and-fling mechanism [10, 12, 14, 16, 17]. In these mechanisms, the unsteady generation of vortices due to flapping and their interaction with the wing play pivotal roles. However, it is important to note that previous research into unsteady lift enhancement mechanisms has typically presumed a smooth wing surface.

1.2.3 Insect wing structure

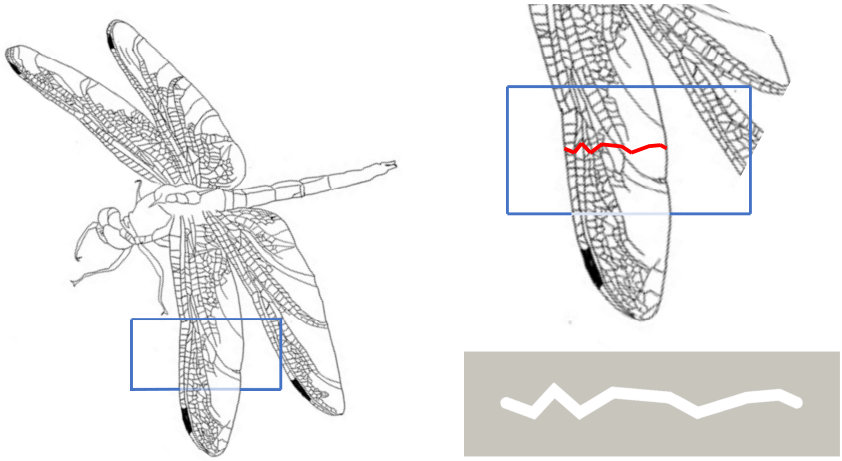

Figure 1: Illustration of dragonfly wing and a corrugated wing model.

This subsection discusses the structure of insect wings. Insects like dragonflies, cicadas, and bees have wings with non-smooth surfaces (Fig. 1). The wings are composed of nerves and membranes, which form cross-sectional shapes defined by vertices (nerves) and line segments (membranes). The wing's overall geometry can be visualized as a linkage of objects that create V shapes or other configurations. Scientists commonly refer to this specific wing type as a corrugated wing [18].

Although the corrugated wing structure is complex, dragonflies' wings share some common features. The wing section exhibits an uneven structure with deeper depth on the leading edge side (in the direction of travel), while the trailing edge side has an uneven structure with less deep depth. The corrugated structure of insect wings becomes more pronounced towards the base and gradually decreases towards the wingtip. Additionally, the V-shape direction at the leading edge is reversed around the middle of the wing [2]. This structure is generally considered to support the wing shape during flapping motion [2, 19, 20] and may also be effective in generating lift.

1.2.4 Experimental and numerical investigations on corrugated wing aerodynamics

When analyzing the aerodynamic characteristics of a wing, it is necessary to determine the angle of attack (AoA), that angle at which the wind meets the wing. Many previous studies of aerodynamic performance on corrugated wings have mainly focused on stationary wings operating in uniform flow conditions at AoAs smaller than 20°, a context associated with gliding flight [2, 21, 22, 23, 24, 25, 26, 27, 28, 29]. The following three paragraphs explain these analysis results.

The lift enhancement mechanism resulting from the corrugated structure was investigated by Newman *et al.* [30] in a range $Re = O(10^4)$, a relatively high Reynolds number within this regime of insect flight. Their experimental setup comprised a model wing with two segments: a corrugated section on the leading edge side and a smoothly curved section on the trailing edge side. The authors suggest that the V-shaped designs in the corrugated wings act as turbulators, causing an early transition to turbulent flow and thus decreasing the separation bubble's size. This flow pattern is recognized for creating increased lift forces [31].

Similarly, Levy *et al.* [25] used the model from Ref. [30] to conduct two-dimensional numerical simulations at Reynolds numbers, $2000 \leq Re \leq 8000$. The study aimed to identify vortex separations resulting from corrugations and their subsequent reattachment, which led to observations of reduced drag and enhanced flight performance.

Vargas *et al.* [28] conducted a two-dimensional numerical simulation using a corrugated model extracted from a dragonfly (referred to as "Profile 2" in Ref. [32]) in a uniform flow at smaller AoAs in the range $[0°, 10°]$, considering Reynolds numbers $Re < 10000$. The results of their analysis highlighted that the aerodynamic performance of the corrugated wing model was comparable to, if not better than, that of the wing that encapsulates the corrugated structure (profiled wing). The study observed that vortices were entrapped within the valleys of the V-shaped corrugations, resulting in a flow pattern similar to that around profiled wings. Other experimental studies [33, 34] and two- and three-dimensional numerical simulations [2, 21] have also documented similar observations of vortex traps.

The investigations outlined below relate to a corrugated wing model subjected to uniform flow with varying AoAs. In measuring the lift coefficient (C_L) and drag coefficient (C_D) for Reynolds numbers $Re = 450, 800$ and 900 across an AoA range from $-22°$ to $50°$, Rees [34] used a corrugated wing model inspired by the hoverfly. The findings indicate that the corrugated wing has a higher C_L than the profiled wing at $Re = 800$. Furthermore, it was observed that the flow characteristics around the corrugated wing were reminiscent of those expected from a wing with an envelope profile.

Similarly, Kesel [32] utilized corrugated wing models inspired by dragonfly wing cross-sections, investigating Reynolds numbers $Re = 7800$ and 10000 across AoAs ranging from $-25°$ to $40°$. The findings indicated that, for certain AoAs, the lift coefficient (C_L) of the corrugated wing model exceeded that of a flat plate.

1.2.5 Characteristics of wing performance in unsteady motion

It has been observed that wings in unsteady motion can generate increased lift at higher AoAs. Dickinson *et al.* [13] analyzed impulsively started flat wings and found lift heightened over time, with maximum lift at AoA = $45°$. The dynamics of the LEV perform an important function [10]. When flat wings are joined by translational motion, an LEV is created [4]. The LEV expands due to its interaction with the vortex sheet that separates from the leading edge [35, 36]. As this occurs, a stagnation point on the upper surface of the wing, caused by the flow directed towards the wing surface by the LEV, gradually moves towards the trailing edge as the LEV advances. Concurrently, the flow on the wing's surface is reversed towards the leading edge between the stagnation point and the leading edge, creating a secondary vortex with the opposite sign to the LEV. In this paper, this secondary vortex is referenced as a "lambda vortex" due to its resemblance to the Greek character "λ" [4, 37]. The LEV separation from the wing takes place when the stagnation point reaches its trailing edge. The expansion of the lambda vortex results in the detachment of the LEV from the wing during eruptions [36, 38]. Following the release of the LEV, the next LEV is then generated.

In the case of corrugated wings, some investigations have focused on their dynamic performance. Luo and Sun [39] carried out three-dimensional numerical simulations with revolving corrugated wing models. Their results showed that the corrugated and flat wings had nearly identical performance. Bomphrey *et al.* [2]

also performed three-dimensional numerical simulations of a flapping wing. Lower pressure was observed in the V-shaped region of the corrugated wing. This finding leads to the conclusion that vortex formation occurs within the V-shaped region and results in a negative pressure area being distributed more widely across the corrugated wing. However, a holistic investigation into the dynamics of the vortices arising from corrugation is currently absent. There is a lack of studies investigating how the interactions between vortices separated from the corrugation structures, the LEV, and the trailing-edge vortex impact lift and drag generation.

In natural situations, dragonflies exhibit wing flapping with high AoAs during most flapping periods [40]. Therefore, the vortex dynamics, including the LEV and other vortices, are crucial for determining aerodynamic performance. However, in the context of corrugated wings, determining whether the vortex motion is caused by the wing structure or the wing motion itself is a significant challenge. Therefore, it is crucial to first understand the flow characteristics around uneven structures.

1.3 Objective of this study

Based on the above considerations, this study initiates an investigation into the flow properties of the uneven structure. Subsequently, the flow characteristics of an unsteady, moving corrugated wing are analyzed. In this specific context, it is necessary to simplify the wing's motion to clarify the dynamic factors that contribute to enhancing the performance of the corrugated wing.

The main objective of this study was to clarify the correlation between the structure of a corrugated wing and the vortex dynamics. A two-dimensional corrugated wing model was used to achieve this objective. Furthermore, the wing motion was simplified and the focus was placed on the generation of unsteady lift resulting from translational motion from a state of rest. Translational motion, along with pitching and rotation, is a crucial aspect of wing motion [4, 41]. This study furthers the comprehension of non stationary mechanisms utilized by insects during dragonfly flight [13]. Although this assumption may omit certain aspects of three-dimensionality and the complex nature of actual flapping motion, they proficiently capture crucial vortex dynamics linked to corrugation. These dynamics involve the generation of vortices from sharp corrugation edges, the leading edge, and the trailing edge, which has not been fully addressed in prior research. The vortex interactions and lift generation outlined in this paper offer valuable insights into investigating particular aspects of the dragonfly wing structure and flapping motion. A similar method was used to analyze flat wings [13, 42, 43, 44], but this was not widely implemented for corrugated wings.

1.4 Outline of this thesis

The structure of this paper is as follows. In Chapter 2, a portion of a corrugated structure with the bottom surface is considered to investigate the characteristics of the flow around the concave-convex structure. In Chapter 3, the flow around a corrugated wing model was analyzed based on real-life dragonfly data. We explored the period focusing on the growth of vortices until their detachment and engagement in mutual interaction. It pays special attention to the influence of the lambda vortex. In Chapter 4, corrugated wing models of different geometries and Reynolds numbers have also been considered. The universality of the relationship between the lift generation mechanism and vortex dynamics in a corrugated wing has been confirmed. The results are summarized in Chapter 5.

Chapter 2

Flow around triangular models

This chapter is based on Ref. [45].

2.1 Introduction

As introduced in Chapter 1, many insects which fly in the low-Reynolds number range of $O(10^2)$-$O(10^4)$ have corrugated wing surfaces. Because the corrugated structure is quite complex, it is crucial to understand the flow characteristics around uneven structures as a first step. This chapter examines the flow characteristics around an uneven structure, using a triangular model as a simple example.

Although the triangle model is a simple shape, flow characters can be complex including the formation of a separation region. The separation region exhibits universal characteristics. The flow speed remains nearly constant in a region close to the separation point between the solid boundary (wall) and the dividing streamline of the separation. This area is commonly known as the dead-water region, which is observed in the backwards-facing step flow [46] or other situations. It is important to note that at high Reynolds numbers ($Re = 2.8 \times 10^4$), the mean flow in the downstream region of a triangular object remains significantly reduced [47]. This alteration in flow characteristics has resulted in diverse flow patterns observed between two cylinders under uniform flow conditions [48].

Based on the above considerations, this chapter investigates two cases. First, the Reynolds number dependency of the flow around one triangular model is investigated. In particular, the flow characters are focused on the Reynolds number region which can be observed in flying insects, $Re \simeq O(10^2)$-$O(10^4)$. Second, the structure dependency of the flow around two triangular models is investigated.

2.2 Method

2.2.1 Triangular model

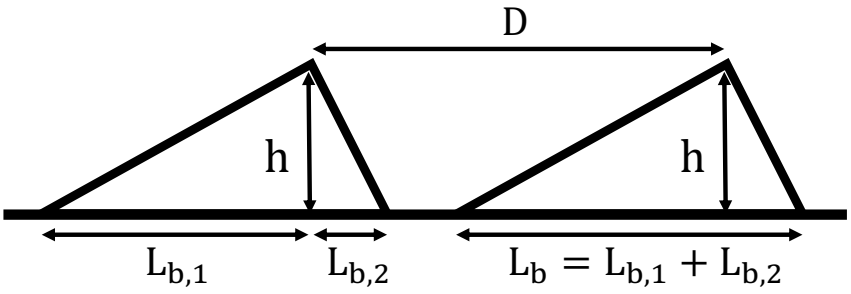

Figure 2: The triangular models.

This analysis is carried out in a two-dimensional space using one or two triangular model(s) illustrated in Fig. 2. A single triangular model has an h peak height. The baseline length, L_b, was divided at the base of the perpendicular from the peak: $L_{b,1}$ and $L_{b,2}$. The bottom lengths were defined as $L_{b,1} = 4h$ and $L_{b,2} = 2h$, resulting in an aspect ratio of $h/L_b = 1/6$. The model will subsequently be referred to as the triangular model.

The following cases were investigated. (1) A single triangular model case. Flow transitions around the single triangular model were focused on at various Reynolds numbers. (2) Two triangular models case. In this case, two identical triangular models are positioned. Two triangular models are considered with a horizontal peak-to-peak distance, D ($6 \leq D \leq 12$) for a single Reynolds number.

2.2.2 Numerical Simulation

The dimensionless, two-dimensional incompressible Navier-Stokes equations are expressed as:

$$\frac{\partial \mathbf{u}}{\partial t} + (\mathbf{u} \cdot \nabla)\mathbf{u} = \frac{1}{\rho}\nabla p + \nu \Delta \mathbf{u}, \quad \nabla \cdot \mathbf{u} = 0. \tag{1}$$

Here, $\mathbf{u} = (u, v)$ represents the velocity, p is pressure, and ρ is the air density. The spectral element method is utilized to perform the numerical calculations [49], where the computational domain was divided into quadrilateral elements with physical quantities represented by polynomial functions, ensuring (C^0) continuity across element boundaries [50]. This approach combines the exponential (spectral) convergence of errors linked with global collocation practices with the geometrical flexibility of usual low-order finite element techniques [51]. To solve Eq. (1), the open-source computational software *Semtex* [51] was utilized. The size of the rectangular computational region was $W \times H$, excluding the triangular models where $h = 1$, $H/h = 5$ and $W/h = 50$. The computational area was divided into $N_v \times N_h$ elements fitted to the boundaries of the surface of the ground, triangular model(s), and computational domain. In this study, $(N_v, N_h) = (100, 10)$ was utilized. The number of Lagrange knot points, N_p, assigned along the side of each element, was 9. The total number of meshes within an element is of the order of N_p^2.

Uniform flow was assumed as $\mathbf{U} = (\mathrm{U}, 0) = (1, 0)$. The boundary conditions were solid boundaries for the ground, $\mathbf{u} = \mathbf{U}$ on the left and top boundary conditions, and outflow conditions applied to the right boundary.

The right side applied reliable outflow conditions recommended in Ref. [52] with a smoothness parameter of 0.1. In this Chapter, the definition of the Reynolds number is based on L_b to correspond with subsequent chapters, i.e., $Re = L_b|\mathbf{U}|/\nu$. In the case of a single triangular model, the Reynolds number ranges are from 600 to 12000. In the case of two triangular models, the Reynolds number is $Re = 6000$. In all calculations, the simulation time was 400 units, and the time step, Δt, was set to 1.0×10^{-3}. The computations were carried out within the range $0 \leq t^* \leq 66.67$, where t^* represents the dimensionless time, i.e., $t^* = |\mathbf{U}|t/L_b$.

Their relationship with the flow field, specifically vorticity, and flow speed fields has been investigated. The vorticity field is defined as $\omega_z = \partial v/\partial x - \partial u/\partial y$, where $\mathbf{u} = (u, v)$.

2.3 Result and discussion

2.3.1 Single triangular model case

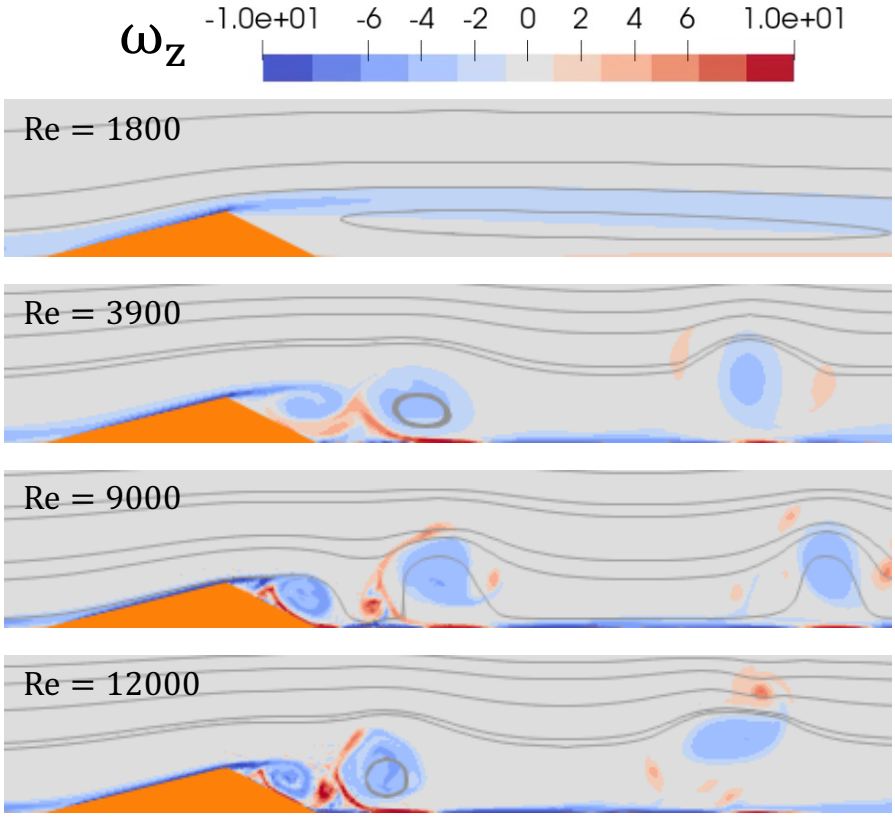

Figure 3: Reynolds number dependence on the vorticity field around the single triangular model (colored orange). Curves are streamlines. Reprinted from Ref. [45], however, Reynolds number is modified because of redefining the typical length.

The flow structures around a single triangular model were analyzed and Reynolds number dependency was examined. In Fig. 3, the flow fields around this model at Reynolds numbers of 1800, 3900, 9000 and 12000 are illustrated. Streamlines are exhibited through curves, while the vorticity field is indicated through colors.

In the Reynolds number regime where $Re < 1800$, a stable flow dominated and transient separation vortex formation was not observed. The speed of the flow downstream of the triangular model was very slow, suggesting a dead-water region.

For Reynolds numbers within the range of $1800 \leq Re < 3900$, an asymptotic steady flow was observed. Nevertheless, due to separation, coherent vortices were generated transiently. The time interval in which coherent vortices are observed until they reach the asymptotic state (equivalent to the transient time) depends on the Reynolds number. As Reynolds number approaches the critical value Re_c, within the range $(3600, 3900)$, transient time becomes very long.

In the range of $3900 \leq Re < 10200$, a periodic flow was observed. The flow generated coherent vortices regularly, resulting in an oscillatory flow. The generation of successive coherent vortices led to a backward flow. The amplitude of oscillation was greater than the characteristic flow speed when $Re \leq Re_c$. Finally, in the range of $10200 \leq Re < 12000$, the flow displayed non-periodic behavior.

The purpose of this study is to investigate the dynamic characteristics of the corrugated wing. The above results are based on a range of $t^* < 66.\dot{6}$ but it is enough to focus on a range of $t^* < 10$ for this study (c.f. Section 3.1). Although the transition time depends on the Reynolds number, vortex motion is observed around the convex structure for a range of $t^* < 10$ in the range of $Re = O(10^3)$.

2.3.2 Two triangular models

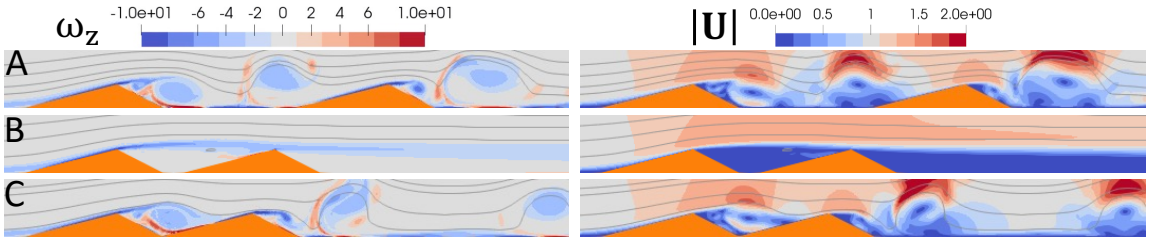

Figure 4: Distance dependence of flow characteristics for two triangular models ($Re = 6000$). Typical flow patterns are displayed; $D = 12, 7, 6$. Reprinted from Ref. [45]

The flow around two triangular models at $Re = 6000$ can be classified into three different patterns, as demonstrated in Fig. 4. The first pattern is the independent case ($9 \leq D$), in which the flow around the models presents minimal interference when D is sufficiently large. The second is the dead-water case ($6.8 \leq D \leq 7.8$), where the asymptotic flow is stable and a dead-water area appears between the triangular models and downstream of the triangular model at the downstream side. The third is the interference case ($6 < D < 6.8$ or $7.8 < D < 9$). Coherent vortices emanate from the peaks of the two triangular models. The vortex generated at the top of the triangular model upstream interferes with the flow on the slope of the triangular model downstream.

Thus, when two triangular models are placed, the flow patterns are more varied than in the case of a single model. The flow pattern depends on the distance between the two models, D, especially the flow

pattern depends on D. The flow structure near the uneven structure of the corrugated wing should be carefully observed.

2.4 Summary

This chapter investigated the flow around triangular models in two-dimensional space, representing the simplest examples of corrugated wing structures.

Two distinct critical Reynolds numbers emerge in the Reynolds number regime of $Re = O(10^3)$, corresponding to transient and steady vortex generation. As many insects exhibit flight in this Reynolds number range, it is expected that vortex motion is induced by the uneven structure of corrugated wings.

In the case of two objects, a dead-water region becomes apparent between them. Such a classification of flow structures remains applicable even at higher Reynolds numbers, where the presence of a dead-water region has also been observed [47]. Since the corrugated wing has many uneven structures, it is necessary to investigate the dependency of its structure.

In the case of two models, the flow becomes more complex, depending on the distance of these. Although vortex dynamics are observed in the case of a single triangular model at $Re = 6000$, a dead-water region is observed between the models, suppressing the formation of vortices from the top of the model. The classification of flow structures based on D is applicable even at higher Reynolds numbers, where dead water regions are also observed [47]. This highlights the flow around concave-convex structure has a strong parameter dependency and the need for investigating models closer to real dragonflies to understand their flight. Additionally, since corrugated wings possess numerous undulations, it is evident that the dependence of corrugated wing structures also needs examination.

Chapter 3

Vortex-corrugation interaction in dynamic lift enhancement mechanism of dragonfly wing

This chapter is based on Ref. [3].

3.1 Introduction

This chapter analyzes the flow around a corrugated wing model, which is based on real-life dragonfly data. Real-life dragonflies fly at low Reynolds numbers ($Re = O(10^3)$), and corrugated wing structures show diversity depending on the individual and where they are sectioned. Therefore, it is difficult to examine all of the variations of corrugated wings. In this chapter, we focus on a single Reynolds number and a single wing model.

Here, the primary interest is to investigate how wing corrugation contributes to enhancing unsteady lift. We investigate the fundamental mechanism due to unsteady wing motion during translational motion from the rest state. This study examines the stage of vortex interaction, which is characterized by the substantial growth of vortices leading to detachment and mutual interaction. Special attentions are paid to exploring the impact of the lambda vortex with the sign opposite to that of LEV.

3.2 Method

3.2.1 Corrugated wing model

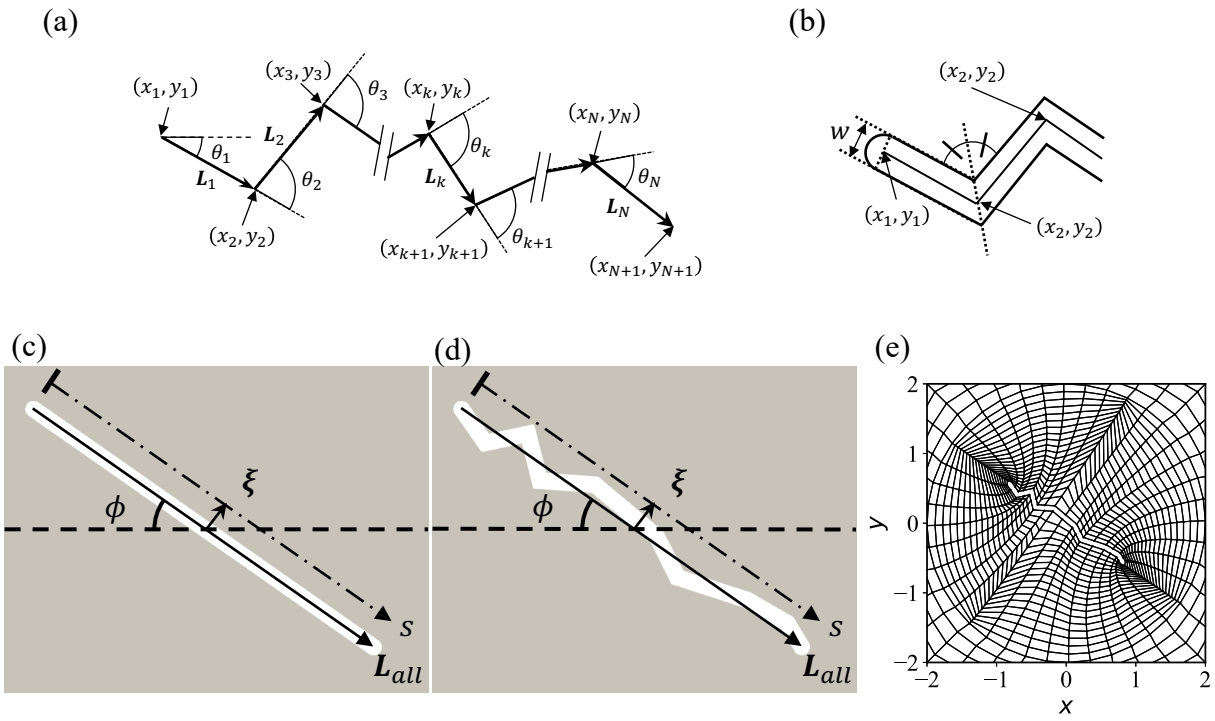

Figure 5: Wing model descriptions. (a) Vertices (x_k, y_k) $(k = 1, \cdots, N+1)$, neighboring displacement vectors $\mathbf{L}_k$, and angles between $\mathbf{L}_k$ and $\mathbf{L}_{k-1}$, θ_k. (b) Line segments, wing model thickness w and the shape of the end. (c) Flat wing model ($\alpha = 0$). (d) Corrugated wing model ($\alpha = 1$). (e) Spectral elements around the corrugated wing model ($\phi = 35°$). Reprinted from Ref. [3].

A two-dimensional model of a corrugated wing was constructed with reference to the real-life dragonfly wing (*Aeshna cyanea*) (Ref. [32], Profile 1). The wing model was constructed using a cross-section with a place vertical to the line between the wing base and wing tip. The position was roughly 30% from the wing base. The leading-edge side exhibits deeper corrugated structures, while the trailing-edge side has less deep (flatter) structures, which is consistent with the corrugated wings of flying insects in nature.

The wing model was generated by adding thickness to N-line segments. The positions of the endpoints were defined as $A = \{(x_k, y_k) \mid k = 1, \cdots, N+1\}$ (see Fig. 5 (a)) and a set of displacement vectors $B = \{\mathbf{L}_k \mid \mathbf{L}_k = (x_{k+1} - x_k, y_{k+1} - y_k); k = 1, \cdots, N\}$. The core shape of the corrugated wing model was determined using set C, which includes line segment lengths and angles between adjacent displacement vectors: $C = \{L_k \mid L_k = |\mathbf{L}_k|; k = 1, \cdots, N\} \cap \{\theta_{k+1} \mid \theta_{k+1} = \cos^{-1}\left[\langle \mathbf{L}_k, \mathbf{L}_{k+1} \rangle / (\mathbf{L}_k \mathbf{L}_{k+1})\right]; k = 1, \cdots, N-1\}$ where $\langle \mathbf{a}, \mathbf{b} \rangle$ is the inner product of vectors $\mathbf{a}$ and $\mathbf{b}$. θ_1 is defined as the angle between the x-axis and $\mathbf{L}_1$ (Fig. 5 (a)).

Once the set C is determined a family of corrugated wing shapes are characterized, by introducing a shape parameter α. This is achieved by replacing θ_k with $\alpha\theta_k$ in set C. This chapter analyzes two cases, $\alpha = 0$ and $\alpha = 1$, correspond to a flat wing (see Fig. 5 (c)), a corrugated wing defined respectively [32] (see Fig. 5 (d)).

The core shape of the corrugated wing model was isotropically rescaled so that the wing chord length, c, is 2, where $c = |\mathbf{L}_{all}|$, and $\mathbf{L}_{all} = \sum_{k=1}^{N} \mathbf{L}_k$. The wing's relative thickness of w/c was 0.04, where w is the wing's thickness (Fig. 5 (b)). The wing core had semicircular ends at $k = 1, N + 1$ (refer to Fig. 5 (b)). The angle between $\mathbf{L}_{all}$ and the x-axis is considered as the AoA, denoted by ϕ.

The study also included an analysis of how pressure and vorticity distributions change over time in a particular region near the upper surface of the wing model. This region is characterized by a distribution that follows a line segment with a shifted vector of $\mathbf{L}_{all}$ by ξ in which $\xi \perp \mathbf{L}_{all}$ (as shown in Figs. 5 (c) and (d)). The line segment's position is determined by s, where $0 \leq s \leq 2$. When $\xi = (0, 0)$, $s = 0$ and 2 correspond to the leading and trailing edges, respectively. The amount of shift $|\xi|$ and s are normalized by the chord length of the wing, that is, $\xi^* = \frac{|\xi|}{c}$, $s^* = \frac{s}{c}$.

3.2.2 Numerical Simulation

The analysis employed the dimensionless, two-dimensional incompressible Navier-Stokes equations, as presented in Eq. (1). To solve Eq. (1), the computational software *Semtex* [51] was utilized. The computational domain was established as $[-30, 30] \times [-30, 30]$, with the wing model centred at $(0, 0)$ (Fig. 5 (e)).

The outer edges of the computational domain, except for the right-hand side ($x = 30, -30 \leq y \leq 30$), were designated as inflow boundaries, with $\mathbf{u} = \mathbf{U}(t^*)$, where $\mathbf{U}(t^*) = (0, 0)$ for $(t^* < 0)$ and $\mathbf{U}(t^*) = (1, 0)$ for $(t^* > 0)$. It is worth noting that the flow acceleration becomes infinite when $t^* = 0$. The values of ν was 5×10^{-4}, resulting in Reynolds numbers $Re = 4000$, based on the chord length c. The time step Δt was fixed at 4.0×10^{-5}, and the computations were carried out within the range $0 \leq t^* \leq 4$, where t^* represents the dimensionless time, i.e., $t^* = |\mathbf{U}|t/c$.

Figure 5 (e) shows the spectral elements surrounding the corrugated wing model at an AoA of $\phi = 35°$. The total number of spectral elements was $N = 2960$, with the discretization of each spectral element by $N_p \times N_p = 19 \times 19$ meshes [51]. Therefore, N_p is the number of points along the edge of each element. To verify the calculation condition, please refer to Ref. [3].

Aerodynamic wing performance was evaluated using the lift coefficient $C_L(\alpha, \phi, t^*) = L/[(1/2)\rho c|\mathbf{U}|^2]$ and drag coefficient $C_D(\alpha, \phi, t^*) = D/[(1/2)\rho c|\mathbf{U}|^2]$, whereby L represents the lift, and D represents the drag. The maximum and mean lift coefficients within the time interval $[a, b]$, denoted as $C_{L,\max}(\alpha, \phi)$ and $C_{L,\text{mean}}(\alpha, \phi)$, respectively, are defined as follows:

$$C_{L,\max}(\alpha, \phi) = \max_{a \leq t^* \leq b} C_L(\alpha, \phi; t^*), \; C_{L,\text{mean}}(\alpha, \phi) = \frac{1}{b-a} \int_a^b C_L(\alpha, \phi; t^*) dt^*, \tag{2}$$

with similar definitions for $C_{D,\text{mean}}$. In particular, the lift is compared between the corrugated wing and the flat wing. The relative difference in $C_{L,\max}$ between the corrugated wing ($\alpha = 1$) and the flat wing ($\alpha = 0$), $\Delta_{\max}$, is defined as follows:

$$\Delta_{\max}(\phi) = \frac{C_{L,\max}(1, \phi) - C_{L,\max}(0, \phi)}{C_{L,\max}(0, \phi)}, \tag{3}$$

and similar definition for $\Delta_{\text{mean}}(\phi)$.

These values are used to characterize the aerodynamic wing performance, and the relationship between pressure fields and vorticity fields was investigated. The pressure was assessed using the pressure coefficient $C_p = \frac{p - p_\infty}{(1/2)\rho c|\mathbf{U}|^2}$, where p is the pressure. The inflow pressure at positions $x = -30$ was p_∞. The vorticity has been normalized as $\omega_z^* = \frac{\omega_z c}{|\mathbf{U}|}$. The flow speed was normalized by a uniform flow same as Chapter 2.

3.3 Result and discussion

This analysis focuses on translational motions from the rest state. However, it is unclear how long period of time is appropriate for this analysis. To answer this question, it is crucial to identify the relevant time scales. The dragonflies under study have a wing chord length of 5-10 mm and flap their wings at a frequency of 36 Hz [40]. Therefore, a single flapping motion takes 1/36s. Dragonflies fly at a speed of 5-10 meters per second [40]. Thus, the time taken for one round of a single flapping motion is at most $t^* < 55$. As this study focuses only on translational motion, an even shorter time is sufficient. This time range ($0 < t^* < 4$) for the simulation represents approximately 10% to 20% of the time for one period of the flapping motion and is considered to correspond to upstroke and downstroke.

The following subsections concentrate on the vortex interaction range ($0.50 < t^* < 3.25$; see Fig. 8 (a)). This range represents the development of the LEV generated on the upper surface of the wing, culminating in the vortices generated close to the wing. Additional information can be referred from Ref. [3].

3.3.1 Wing performance

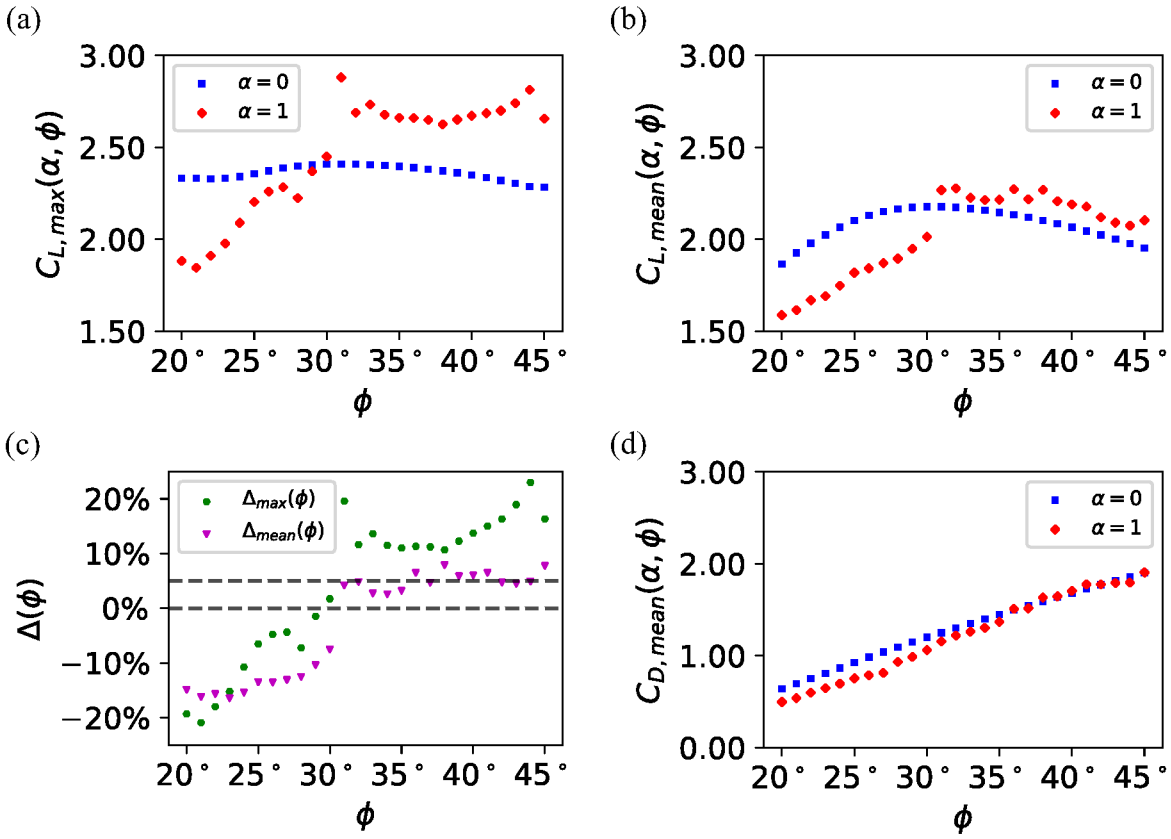

Figure 6: (a) $C_{L,\max}$ during $0.5 < t^* < 3.25$ for the flat wing (blue; $\alpha = 0$) and the corrugated wing (red; $\alpha = 1$). (b) $C_{L,\mathrm{mean}}$ during $0.5 < t^* < 3.25$ for the flat wing (blue; $\alpha = 0$) and the corrugated wing (red; $\alpha = 1$). (c) $\Delta_{\max}$ and Δ_{mean} during $0.5 < t^* < 3.25$. The vertical axis is in percentage form. The dashed lines indicate 0% and 5%. (d) $C_{D,\mathrm{mean}}$ during $0.5 < t^* < 3.25$ for the flat wing (blue; $\alpha = 0$) and the corrugated wing (red; $\alpha = 1$). Reprinted from Ref. [3].

Figures 6 (a) and (b) demonstrate that the values of $C_{L,\max}$ and $C_{L,\mathrm{mean}}$ for the corrugated wing are smaller than those of the flat wing when $\phi < 30°$. Nonetheless, the values of $C_{L,\max}$ and $C_{L,\mathrm{mean}}$ for the corrugated wing surpass those of the flat wing when $\phi > 30°$. These graphs imply a crucial transition in lift coefficients between the corrugated wing and flat wing at approximately $\phi \simeq 30°$. The performance of the corrugated wing improves significantly within the AoA range of $30° < \phi (\leq 45°)$. During this range, the mean value of $\Delta_{\max}$ is 0.14, and the mean value of Δ_{mean} is 0.05. In contrast, the deteriorated case $(20° \leq) \phi < 30°$ had a mean value of Δ_{mean} of -0.14.

In Fig. 6 (d), the graph displays $C_{D,\mathrm{mean}}$ against ϕ. No clear shifts in values are observed. For $\phi > 35°$, the values of $C_{D,\mathrm{mean}}$ are almost identical for both the corrugated wing and the flat wing. However, $C_{D,\mathrm{mean}}$

for the corrugated wing is smaller than that for the flat wing at $\phi < 35°$. As a result, the lift-to-drag ratio L/D follows the same qualitative trend as C_L. From this point forward, the focus will be on using C_L as a measure of wing performance.

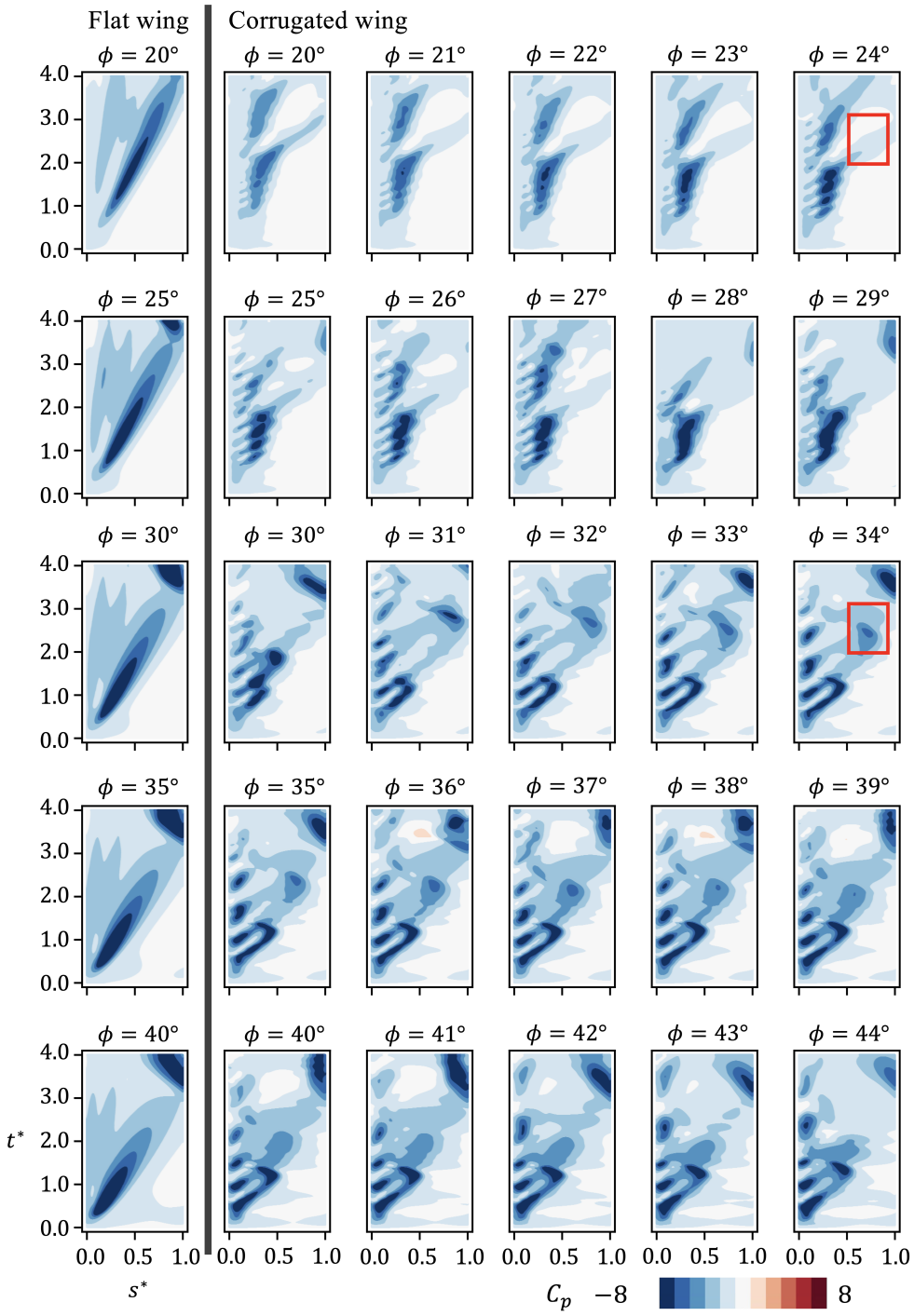

Figure 7: Spatial and temporal distributions of the pressure field are presented with $\xi^* = 0.15$. The s^*-axis represents the horizontal axis, while the t^*-axis represents the vertical axis. Reprinted from Ref. [3].

The pressure fields above the wing can be correlated with the signs of $\Delta_{\max}$ and Δ_{mean}, as detailed below. Figure 7 depicts pressure's spatiotemporal distributions on (t^*, s^*), $(0 \le t^* \le 4, 0 \le s^* \le 1)$ for $\xi^* = 0.15$. The parameter $\xi^* = 0.15$ was chosen to provide a clear result without interfering with the model for observing the vortex motion. The pressure distributions for flat wing cases at $\phi = 20°, 25°, 30°, 35°$ and $40°$ are displayed in the leftmost column. The five columns on the right display the distributions for the indented wing within the range of 20° to 44°.

When the wing performance is improved ($30° \le \phi$; see Fig. 7), low-pressure regions appear near the leading-edge side periodically ($0.0 < s^* < 0.2$, $0.0 < t^* < 2.0$). Such periodic regions are not present in the flat wing ($\alpha = 0$) or the corrugated wing without improved performance ($\alpha = 1$, $\phi < 30°$). Additionally, low-pressure regions appear on the trailing-edge side ($0.5 \le s^*$) during $2 < t^* < 3.25$. This pattern was insensitive to ξ^* [3].

3.3.2 Instantaneous pressure field analysis for lift enhancement

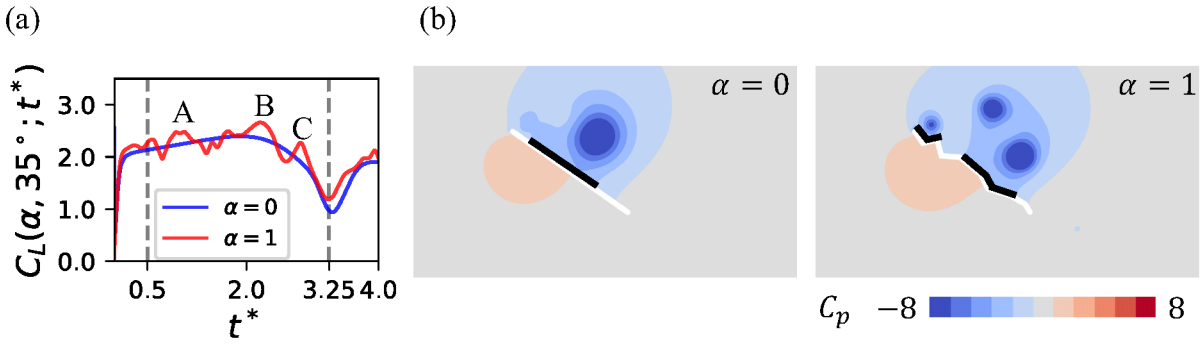

Figure 8: (a) The time series of the lift coefficient is depicted, with the flat wing ($\alpha = 0$) in blue and the corrugated wing ($\alpha = 1$) in red, considering in $\phi = 35°$. (b) Snapshots of the pressure field around the corrugated wing are at $t^* = t^*_{\max}$. Reprinted from Ref. [3].

The case of $\phi = 35°$ was selected as the representative condition to enhance wing performance of the corrugated wing since the values of $C_{L,\max}$ and $C_{L,\mathrm{mean}}$ are similar for $33° \le \phi \le 43°$ (refer to Figs. 6 (a) and (b)). Thus, the vortex dynamics discussed below may be considered a typical mechanism for improving dynamic lift.

Figure 8 (a) shows lift coefficients $C_L(\alpha, 35°; t^*)$ for the flat wing ($\alpha = 0$) and the corrugated wing ($\alpha = 1$). For the flat wing, a singular peak occurs at $t^* \simeq 1.89$, whereas for the corrugated wing, multiple peaks are observed due to oscillations around the $C_L(0, 35°; t^*)$ curve (Fig. 8 (a)). Hence, $C_L(1, 35°; t^*)$ demonstrating oscillatory behavior, highlights intricate interactions between the wing and the vortices. In subsequent analysis, three main peaks were identified, labelled as A, B, and C, for $C_L(1, 35°; t^*)$. $t^*_{\max}$ denotes the time that corresponds to the highest value of $C_L(\alpha, 35°; t^*)$. For the flat wing ($\alpha = 0$), $t^*_{\max}$ is 1.89, whereas for the corrugated wing ($\alpha = 1$, corresponding to peak B), $t^*_{\max}$ is 2.21.

Figure 8 (b) illustrates the pressure fields at $t^* = t^*_{\max}$, where pressure fields are indicated by the pressure coefficient, C_p (Sec. 3.2.2). On the upper wing surface, the low-pressure regions of the corrugated wing are distributed over a larger range in comparison to those of the flat wing. Areas where $C_p \le -\frac{24}{11}$ are designated

by thick black lines. On the lower surface of the wing, the corrugated design displays a more extensive high-pressure region than the flat wing. At maxima A and C, equivalent pressure distributions were observed (data not shown).

3.3.3 The role of lambda vortex in vortex dynamics for lift generation

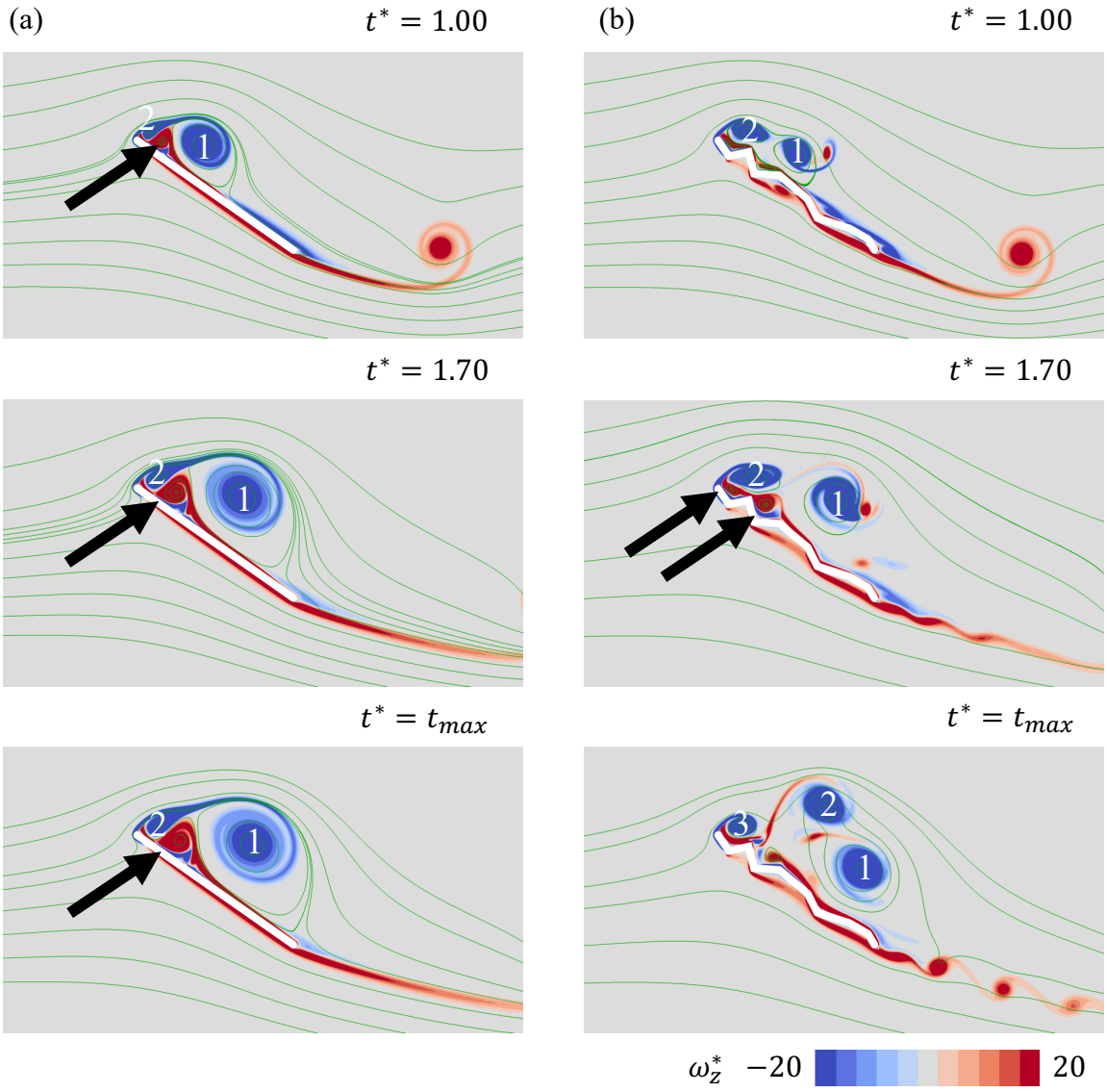

Figure 9: Snapshots of the normalized vorticity fields ($\phi = 35°$) are presented for (a) the flat wing at $t^* = 1.00$, $t^* = 1.70$, and $t^* = t^*_{\max}$, and (b) the corrugated wing at $t^* = 1.00$, $t^* = 1.70$, and $t^* = t^*_{\max}$. Reprinted from Ref. [3].

The essential vortex dynamics contributing to the enhancement of wing performance are outlined below.

Figure 9 (a) depicts the vorticity fields present around a flat wing ($\alpha = 0$). Two snapshots were selected at

$t^* = 1.00$ and 1.70 to illustrate the vortex dynamics that occurred before $t^* = t^*_{\max}$. At $t^* = 1.00$, two negative vortices emerged from the leading edge and were labelled 1 and 2, while a positive secondary vortex appeared in between them, as indicated by the arrow. This secondary vortex is known as a lambda vortex in previous study [4, 13, 36].

Vortex 1 grows continuously by absorbing a vorticity-containing mass [36], while the lift coefficient C_L increases until it reaches its maximum. During this phase, the three vortices keep their relative configurations, causing the centre of Vortex 1 to move away from the wing. At the same time, the point of stagnation resulting from the flow that impinges on the wing's surface shifts downstream, arriving roughly at the trailing edge. This result is in line with the results of previous studies (Ref. [4, 36]). Regarding the pressure distribution, the low-pressure region at the centre of vortex 1 relocates away from the wing. Consequently, the lift generation process becomes monotonous, and the (local) maximum is observed only once within the vortex interaction range.

The uneven structure of the corrugated wing results in significant differences in the behavior of the lambda vortex in comparison with that on the flat wing. The vortex collapses, fragments into several smaller vortices, and becomes entrapped within the V-shaped regions of the wing (see Fig. 9 (b), $t^* = 1.70$, indicated by arrows). As a consequence, the lambda vortex's behavior brings a new element to the unstable vortex dynamics linked with insect flight mechanisms, as explained below.

Figure 9 (b) illustrates the vorticity field around the corrugated wing ($\alpha = 1$). At $t^* = 1.00$, two vortices with negative signs form near the leading edge, labelled 1 and 2. These vortices initially separate from the leading edge, similar to the scenario observed in the flat wing ($\alpha = 0$). Notably, vortex 1 detaches from the vortex sheet connected to the leading edge, followed by vortex 2 shortly after $t^* = 1.70$. Consequently, vortices 1 and 2 function as independent entities, marking a significant departure from the behavior observed in the case of the flat wing. As a result, the relative positions of the vortices at $t^* = t_{\max}$ differ considerably from those in the flat wing case (Fig. 9 (b)).

As a result, vortex 2, being the closest to vortex 1, transports vortex 1 downward toward the wing surface. In contrast to the flat wing case, the collapse of the lambda vortex prevents it from influencing the motion of vortex 1. The proximity of vortex 1 leads to an expanded low-pressure region at $t^* = t^*_{\max}$ (maximum B) (Fig. 9 (b); compare with Fig. 8 (b) for the pressure field).

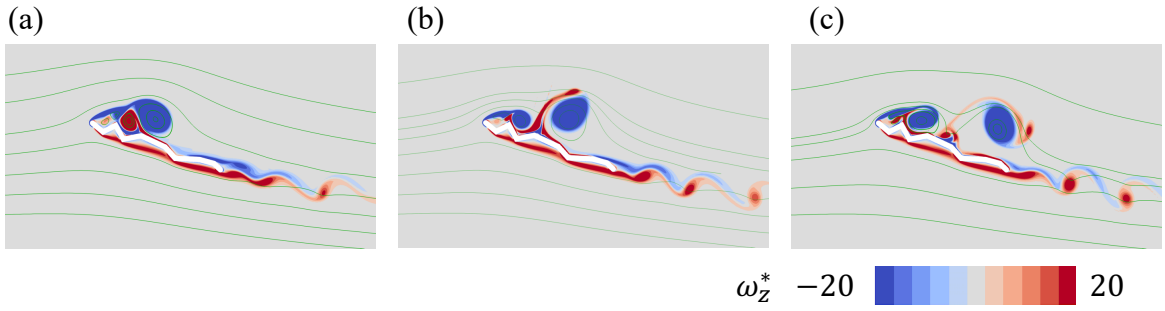

Figure 10: Representative snapshots of the normalized vorticity fields surrounding the corrugated wing ($\alpha = 1$, $\phi = 20°$). (a) $t^* = 2.15$. (b) $t^* = 2.45$. (c) $t^* = 2.81 = t^*_{\max}$. Reprinted from Ref. [3].

The case of $\phi = 20°$ was selected as a typical example of the unimproved performance of the corrugated

wing, due to the similarity in the Δ_{mean} values between 20° and 28° (refer to Fig. 6 (c)). Snapshots portraying the vorticity field of this situation are compared with those representing $\phi = 35°$ (refer to Fig. 9), which exhibits increased wing performance. The lambda vortex appears on the upper surface of the wing (refer to Fig. 10 (a)) when the wing performance is not increased ($\phi \leq 30°$). Subsequently, the elongation of the lambda vortex interferes with the larger LEV and prevents it from being entrained towards the wing, as illustrated in Figs. 10 (b) and (c).

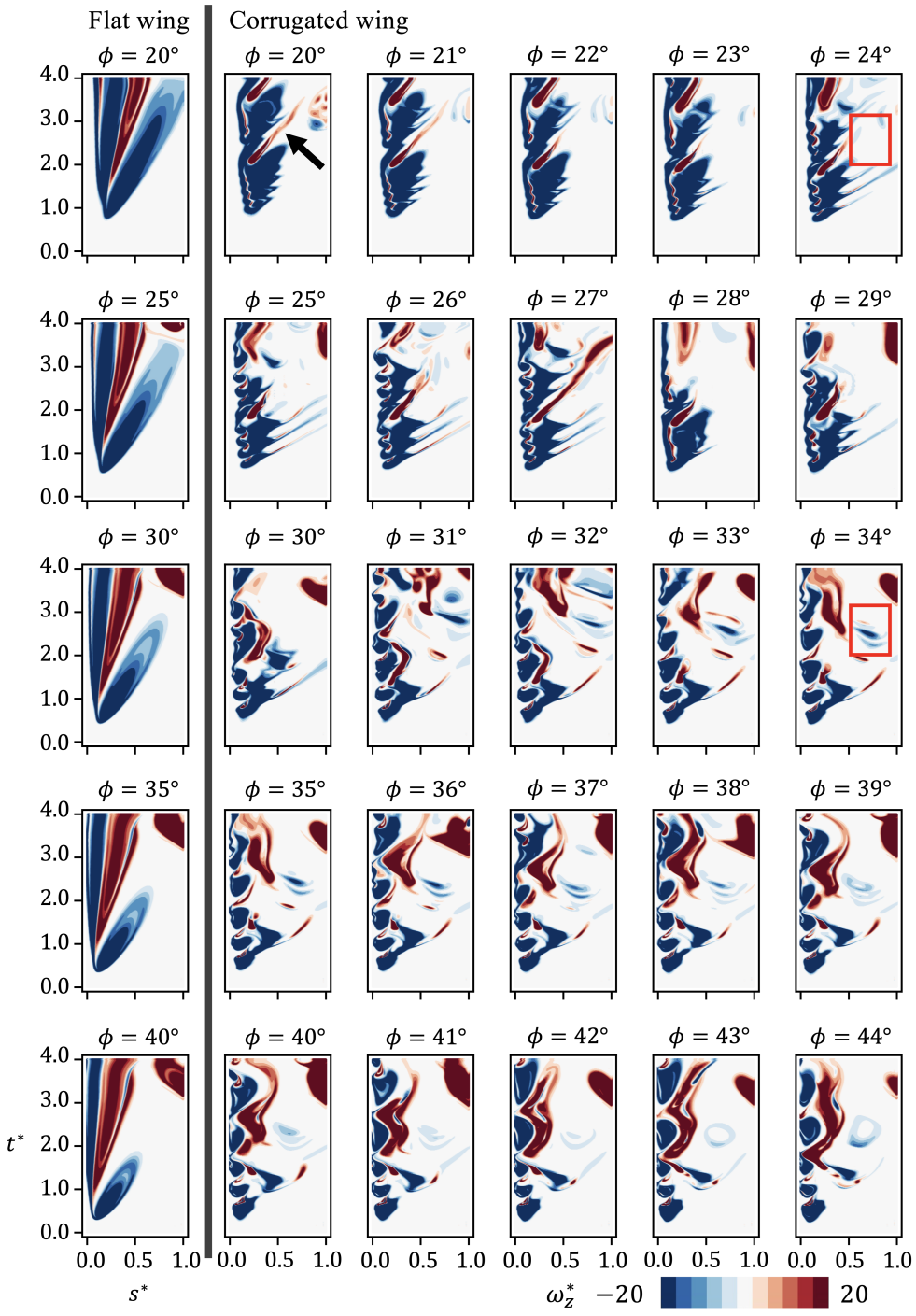

Figure 11: Spatial and temporal distributions of the vorticity field are depicted with $\xi^* = 0.15$. The s^*-axis represents the horizontal axis, and the t^*-axis represents the vertical axis. Reprinted from Ref. [3].

In both scenarios, whether there was an enhancement in the wing performance of the corrugated wing or not, the aforementioned vortex dynamics remained consistent. The spatiotemporal distribution of vorticity on (t^*, s^*), where $0 \leq t^* \leq 4$ and $0 \leq s^* \leq 1$, with $\xi^* = 0.15$, is illustrated in Fig. 11. The leftmost column displays the distributions for the flat wing cases at $\phi = 20°, 25°, 30°, 35°$ and $40°$, while the subsequent five columns depict the same for the corrugated wing within the range of $20° \leq \phi \leq 44°$.

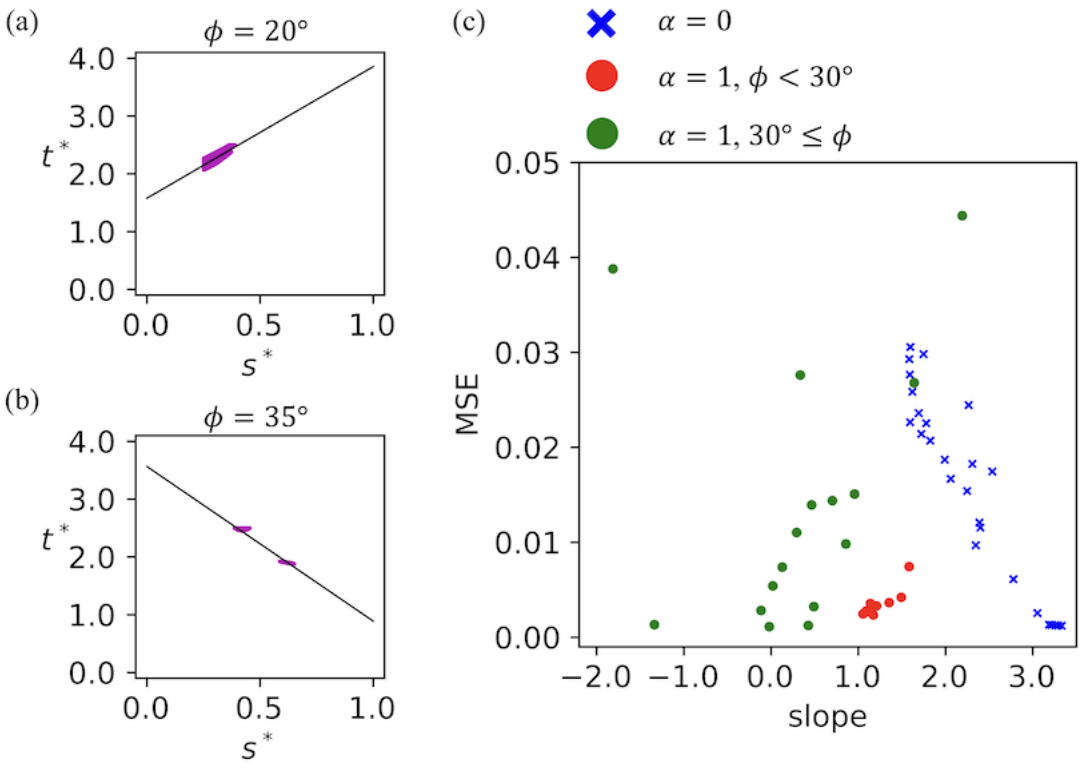

Figure 12: Identification of lambda vortex eruptions. (a) The corrugated wing ($\alpha = 1, \phi = 20°$). (b) The corrugated wing ($\alpha = 1, \phi = 35°$). (c) Outcomes of linear regression for the lambda vortex distribution. Phase diagram illustrating the relationship between slope and MSE. Reprinted from Ref. [3].

The appearance of the lambda vortex is signaled by a positive-signed vortex detected at $t^* = 2, s^* = 0.25$ (indicated by the arrow in $\phi = 20°$ in Fig. 11). This eruption subsequently drives the vortex towards the trailing edge over time (compare with Fig. 10). As a result, the lambda vortex enlarges along the s^*-axis from a particular moment, as demonstrated by the recording of positive-signed vorticity. Moreover, the positive-signed vorticity translates in a positive direction on the s^*-axis as time progresses, due to the underlying flow. To measure the vortex eruption, a vorticity field is isolated for linear fitting using the least-squares method, meeting the requirement $s^* > 0.25, 1.5 < t^* < 2.5, \omega_z^* \geq 20$. For example, Figs. 12 (a) and (b) demonstrate the extracted areas (magenta) and fitted lines for the corrugated wing at $\phi = 20°$ and $35°$, respectively. This method enabled the detection of elongated vortices. Figure 12 illustrates the plotted mean squared error (MSE) of the fit and the gradient of the regression line.

When there is no improvement in wing performance (Fig. 12 (c); red circle), the slope tends to be around

1, and the MSE is confined and small. This implies that the positively-signed vortex moves towards the trailing edge, which indicates the lambda vortex eruption. In contrast, when there is an improvement in wing performance (Fig. 12 (c); green circles), the slope is either small or shows substantial variation, with the results depending on ϕ. Under these circumstances, no distinct lambda-vortex eruption can be observed.

In the context of the flat wing (Fig. 12 (c); blue cross), the slope is concentrated within a range greater than 1. This observation suggests the movement of a vortex with a positive sign toward the trailing edge in the specified region, corresponding to the manifestation of a lambda vortex eruption.

In corrugated wings with $30^\circ \leq \phi$, vortices displaying negative signs are periodically generated on the leading-edge side, as depicted in Fig. 11. This observation aligns with the pressure-field outcomes illustrated in Fig. 7. This pattern was insensitive to ξ^* [3].

3.3.4 Mean behavior

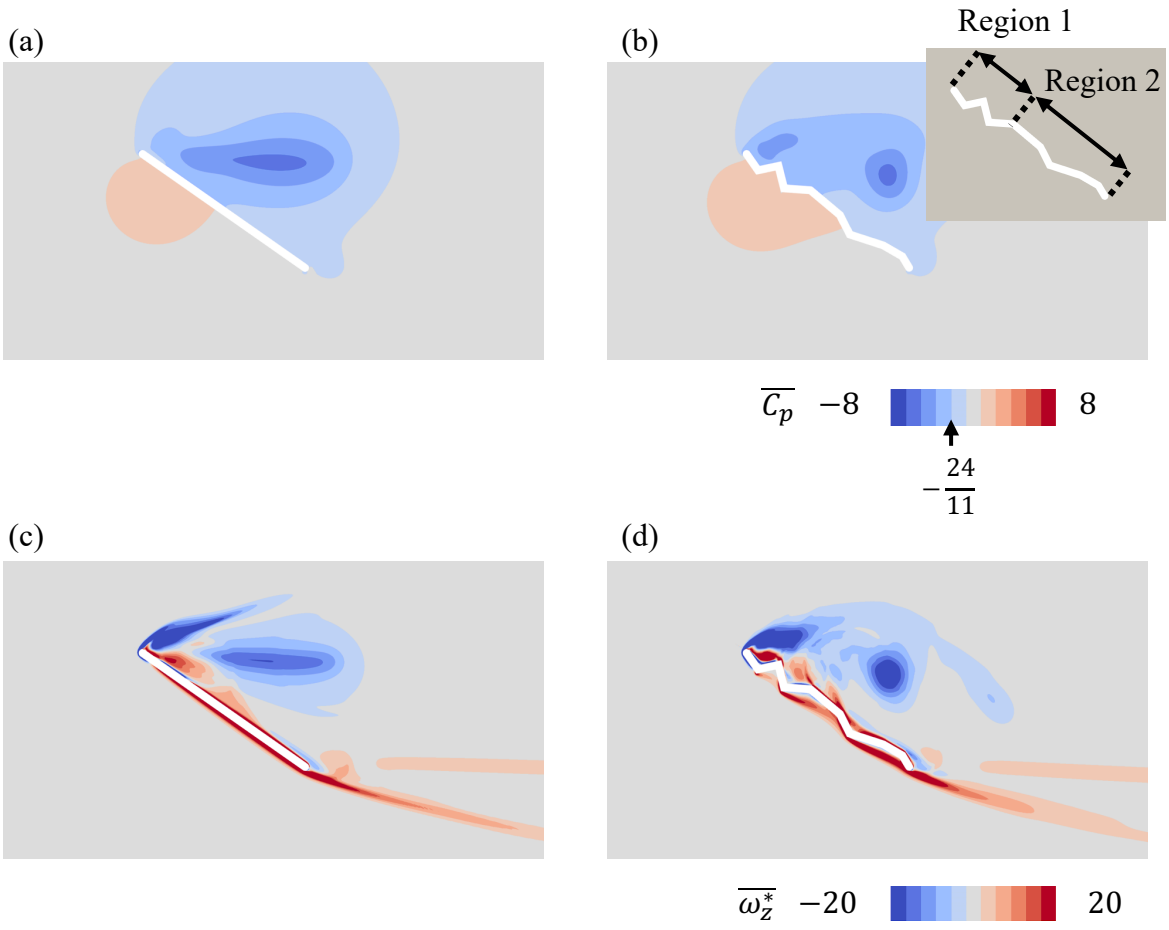

Figure 13: Mean pressure fields around (a) the flat wing ($\alpha = 0$, $\phi = 35°$) and (b) the corrugated wing ($\alpha = 1$, $\phi = 35°$), along with the delineation of the region around the corrugated wing model to comprehend flow characteristics. Mean normalized vorticity fields around (c) the flat wing ($\alpha = 0$, $\phi = 35°$) and (d) the corrugated wing ($\alpha = 1$, $\phi = 35°$). Reprinted from Ref. [3].

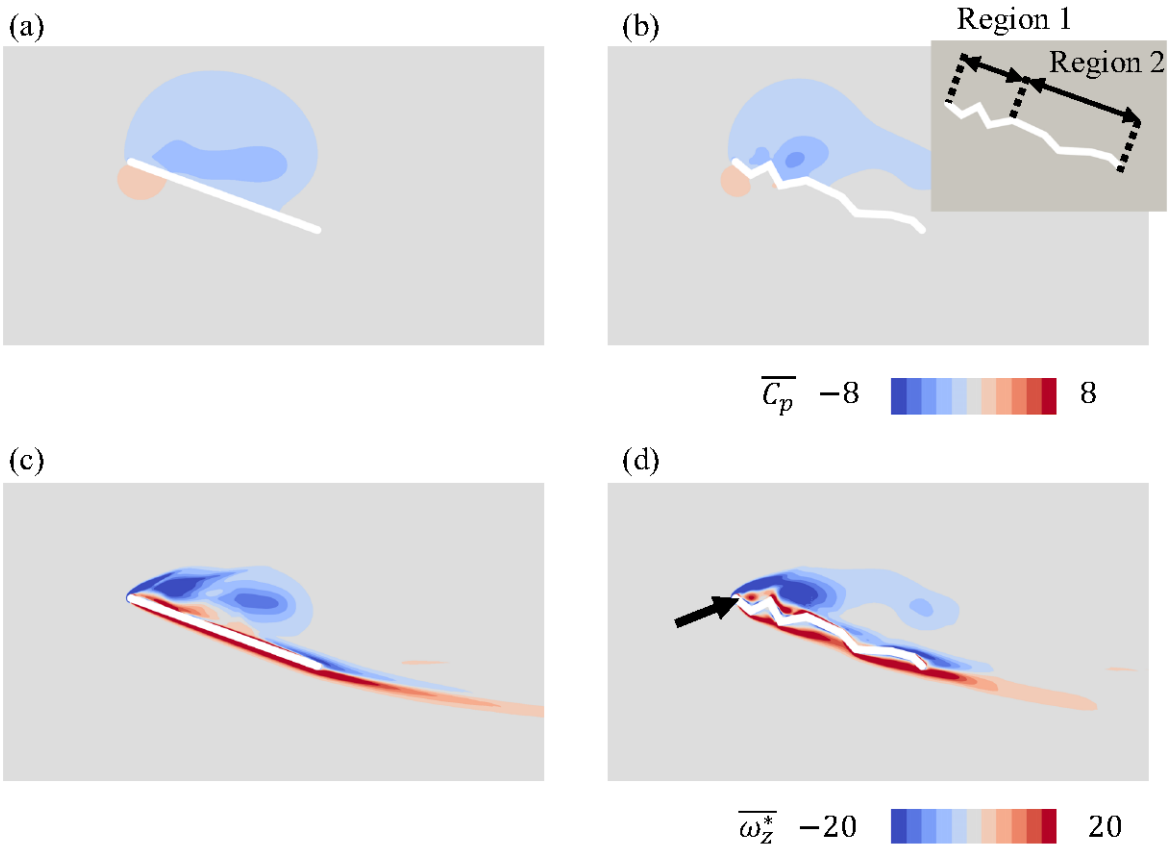

Figure 14: Mean pressure fields around (a) the flat wing ($\alpha = 0$, $\phi = 20°$) and (b) the corrugated wing ($\alpha = 1$, $\phi = 20°$), along with the delineation of the region around the corrugated wing model to comprehend flow characteristics. Mean normalized vorticity fields around (c) the flat wing ($\alpha = 0$, $\phi = 20°$) and (d) the corrugated wing ($\alpha = 1$, $\phi = 20°$). Reprinted from Ref. [3].

In this section, our attention is devoted to examining the mean flow behavior of the corrugated wing within the vortex interaction range ($0.50 < t^* < 3.25$). The aim is to shed light on the mechanism behind lift enhancement. A comparison is made between two scenarios: $\phi = 35°$, where lift enhancement is observed, and $\phi = 20°$, where it is not. The mean pressure and vortex fields are displayed in Fig. 13 (case $\phi = 35°$) and Fig. 14 (case $\phi = 20°$). Additionally, two distinct regions are delineated: Region 1, which is the upper side near the leading edge, and Region 2, which is the remaining portion of the wing. These regions are depicted in the insets of Figs. 13 (b) and 14 (b). Region 1 includes two V-shaped spaces, with the boundary marked by (x_5, y_5).

The behaviors in Regions 1 and 2 are analyzed separately. On the corrugated wing in Region 1, there was a negative pressure area that had a larger width compared to the flat wing when $\phi = 35°$ (see Figs. 13 (a) and (b), particularly where $C_p \leq -\frac{24}{11}$). This negative pressure area was linked to a vortex region of positive sign that was restricted within the V-shaped area (Fig. 13 (d)), resulting from the lambda vortex collapse. Further

details are provided in Section 3.3.5.

In contrast, for the case of $\phi = 20°$, both wings displayed similar negative pressure distributions in this area (refer to Figs. 14 (a) and (b)). The region of higher negative pressure (where $C_p \leq -\frac{24}{11}$) did not expand beyond the wing surface (Fig. 14 (b)) attributable to the smaller size of the rounded vortex (Fig. 14 (d); indicated by the arrow).

In Region 2, both wings had similar pressure distributions at $\phi = 35°$. Figures 13 (a) and (b) illustrate this observation. A circular configuration of vorticity distribution was observed on the corrugated wing, with the LEV persisting over a specific time interval (Fig. 13 (d)). In contrast, the vorticity region for the flat wing experienced elongation because of comparable LEV development (Fig. 13 (c)).

At $\phi = 20°$, the negative pressure region on the flat wing surpassed that on the corrugated wing (see Figs. 14 (a) and (b)), which is in line with the negative value of Δ_{mean} (see Fig. 6 (c)). Conversely, for the corrugated wing, the circular vorticity region identified in the $\phi = 35°$ instance transitioned towards the leading-edge side. No discernible vorticity region was evident in this region (Fig. 14 (d)), resulting in the narrower negative pressure region (Fig. 14 (b)). On the other hand, the vortex area for the flat wing stayed comparatively near the wing surface, retaining the detrimental pressure area (Fig. 14 (a)).

In summary, a thorough investigation was conducted into the increase in average lift, focusing on two distinguishable sections. The flow showcased near-constant features on the lower part of the wing, and the theoretical concept of a 'profiled wing' applied to all scrutinized ϕ values, despite earlier research predominantly encompassing smaller AoAs [25, 28]. Nevertheless, the complex behavior of vortices on the upper surface was crucial to evaluating lift production. On occasions where the wing with corrugations showed increased lift, the LEV persisted very close to the wing, requiring interference mitigation by the lambda vortex. The corrugations disturbed the lambda vortex, entangling it in V-shaped regions. Further investigation into the dynamics surrounding the leading edge is necessary, as outlined in the following subsection.

3.3.5 Generation of low pressure region in vortex dynamics near the leading edge

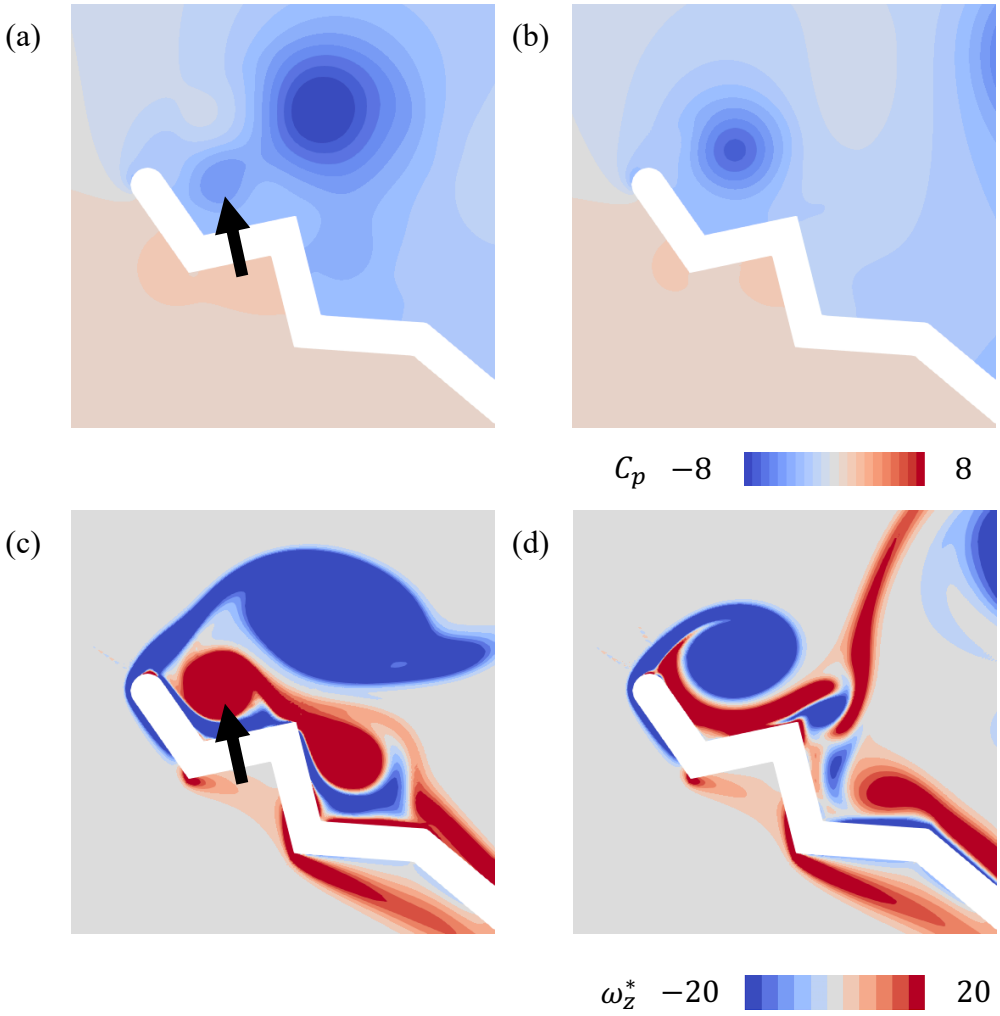

Figure 15: Representative snapshots of the flow field in the vicinity of the leading edge of the corrugated wing ($\alpha = 1, \phi = 35°$). Pressure fields at (a) $t^* = 1.80$ and (b) $t^* = 2.15$. Vorticity fields at (c) $t^* = 1.80$ and (d) $t^* = 2.15$. Reprinted from Ref. [3].

This subsection explains the generation of mean low pressure in the V-shaped region resulting from the collapse of the lambda vortex and LEV in the corrugated wing (refer to Fig. 13 (b)).

Let us compare the position of the low-pressure area at $t^* = t^*_{\max}$ (Figs. 8 (b) and (c)) with the mean fields (Figs. 13 (a) and (b)). On the top side of the wing, the corrugated wing displays a distinct low-pressure region in the first V-shaped region near the leading edge (Fig. 13 (b)). This low-pressure region is not present in the

second V-shaped region (Fig. 13 (a)). On the other hand, the level wing exhibits a considerable region of low pressure located at a specific distance from the leading edge. It is worth noting that the low-pressure region on the wing is caused by the proximity of the vortex, as explained in Sec. 3.3.2 (Fig. 8 (b)), and it is not visible in the mean-field (Fig. 13 (b)). On the contrary, the low-pressure region in the first V-shaped region is only a snapshot when the maximum lift is achieved (Figs. 8 (b) and 9).

Figure 15 displays the flow fields of the corrugated wing ($\alpha = 1$) at $t^* = 1.80$ and 2.15, selected to evaluate the wing performance near the leading edge in relation to the mean flow field. This evaluation aims to ensure clarity about the two typical vortex dynamics outlined below.

Figures 15 (a) and (c) display the pressure and vorticity fields for $t^* = 1.80$. A vortex with negative polarity comes from the leading edge, and a secondary vortex with positive polarity forms due to the collapse of the lambda vortex and sits between the wing and the vortex (indicated by the arrow in Fig. 15 (c)). This leads to a low-pressure region emerging in the first V-shaped region (indicated by the arrow in Fig. 15 (a)).

Figures 15 (b) and (d) depict the pressure and vorticity, respectively, at the time $t^* = 2.15$. Here, a vortex with a positive sign experiences compression (Fig. 15 (d)), resulting in a low-speed area. Within the leading-edge concavity, a positively signed vortex creates a dead-water region that undergoes transmission and transfers negative pressure from the LEV to the wing surface (Fig. 15 (b)).

As previously discussed, the dynamics within the initial V-shaped region exhibit non-stationary behavior. However, the interaction between round vortices, which display both positive and negative signs, leads to the formation of a mean low-pressure region. The periodic generation of vortices with opposing signs is also apparent in Figs. 7 and 11. This phenomenon persists even after temporal averaging, as shown in Fig. 13.

3.4 Summary

This chapter conducted a detailed analysis of the flow around a two-dimensional corrugated wing model through direct numerical simulations at $Re = 4000$, comparing its performance with that of a flat wing. Notably, the corrugated wing exhibited enhanced performance, particularly when the AoA exceeded 30°.

The uneven structure of the corrugated wing induces higher lift force due to intricate flow patterns and vortex dynamics. In this context, two mechanisms that enhance lift are explored, attributable to the uneven structure of a singular corrugated wing, modeled after a dragonfly.

The first mechanism involves a decrease in pressure on the upper surface of the corrugated wing, attributed to interactions among vortices disassociated from the leading edge. The detachment and formation of these vortices result from the collapse of the lambda vortex.

The second mechanism entails the dynamic formation of a mean low-pressure region within the V-shaped structure near the leading edge on the upper surface of the corrugated wing. In this scenario, the collapsed lambda vortices and the LEV adhered to the V-shaped region near the leading edge create a negative pressure area, resulting in the formation of an averaged low-pressure region. To the best of my knowledge, these dynamic mechanisms have not been previously documented. The findings present a crucial foundation for investigating the mechanisms of insect flight.

Chapter 4

Vortex dynamics and lift enhancement: difference among corrugated structures and Reynolds numbers

This chapter is based on Ref. [37].

4.1 Introduction

Previous research [4] has established the occurrence of a secondary vortex, called the lambda vortex, in the case of flat wings. On the other hand, corrugated wings demonstrate the collapse of the lambda vortex due to uneven structures. This phenomenon enhances the wing performance of the corrugated wing, particularly in terms of lift (Chapter 3).

However, in Chapter 3, only a single corrugated wing model at a single Reynolds number ($Re = 4000$) was analyzed. To investigate whether the correlation between the lambda vortex and lift enhancement is universal, it is necessary to investigate other models at other Reynolds numbers. It is noteworthy that the concavity of the corrugated structure in dragonflies' corrugated wing depends on the selected cross-sectional position (Chapter 1).

This chapter also examines the aerodynamic performance of translating two-dimensional corrugated wing over a defined period. The study focuses on two corrugated wing models with different quantities of V-shaped structures near the leading edge. The relationship between wing performance and lambda vortex behavior at different Reynolds numbers is also investigated. The lambda vortex behavior, as discussed in Chapter 3, will be shown as a crucial factor in evaluating and categorizing dynamic wing performance across various models.

4.2 Method

4.2.1 Corrugated wing model

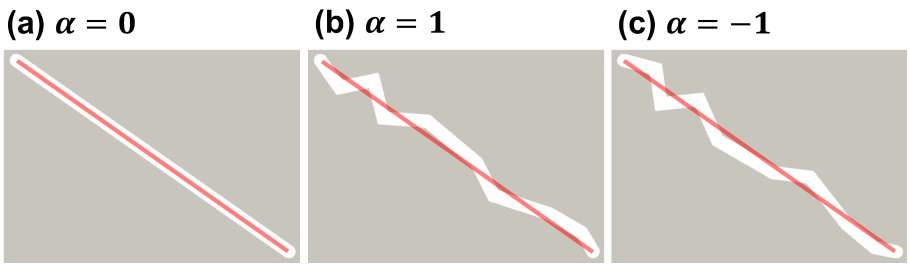

Figure 16: (a) Flat wing model ($\alpha = 0$). (b) Corrugated wing model ($\alpha = 1$). (c) Inverted corrugated wing model ($\alpha = -1$). Reprinted from Ref. [37].

Wing models are constructed using the methods described in 3.2.1. This chapter analyzes three different wing model cases which are characterized by a structure parameter, α. A structure parameter, α, of -1, 0, and 1 corresponds to a flat wing (Fig. 16 (a)), a corrugated wing defined concerning Ref. [32] (Fig. 16 (b)), and an inverted corrugated wing with a shape opposite to that of the corrugated wing model for $\alpha = 1$ (Fig. 16(c)). A flat wing ($\alpha = 0$) and a corrugated wing ($\alpha = 1$) are the same as that in Chapter 3.

4.2.2 Numerical Simulation

The calculation methods are generally similar to those described in Chapter 3. The differences are described below. The computational domain was established as $[-10, 10] \times [-10, 10]$, with the wing model centred at $(0, 0)$. The outer edges of the computational domain, except for the right-hand side ($x = 10, -10 \leq y \leq 10$), were designated as inflow boundaries, with $\boldsymbol{u} = \boldsymbol{U}(t^*)$. The outflow conditions on the right side were applied in the same way as described in Chapter 3. This investigation set the values of $\nu = 5 \times 10^{-4}$ or 1.3333×10^{-3}, resulting in Reynolds numbers $Re = 4000$ or 1500, respectively. The time step Δt was fixed at 4.0×10^{-5}, and the computations were carried out within the range $0 \leq t^* \leq 4$, where t^* represents the dimensionless time, i.e., $t^* = |\boldsymbol{U}|t/c$. The total number of spectral elements was $N = 1960$. The number of points along the edge of each element was $N_p = 19$. To verify the calculation condition, please refer to Ref. [37].

The maximum and mean lift coefficients in the time interval $[a, b]$ were defined the same as Eq. 2, however, Reynolds number is added to the argument. Thus, $C_{L,\max}(\alpha, \phi, Re)$ and $C_{L,\mathrm{mean}}(\alpha, \phi, Re)$ were indicated, respectively. Relative differences are defined in the same i.e., $\Delta_{\max}(\alpha, \phi, Re)$, $\Delta_{\mathrm{mean}}(\alpha, \phi, Re)$.

4.3 Result and discussion

4.3.1 Wing performances of corrugated wings at $Re = 1500$ and $Re = 4000$

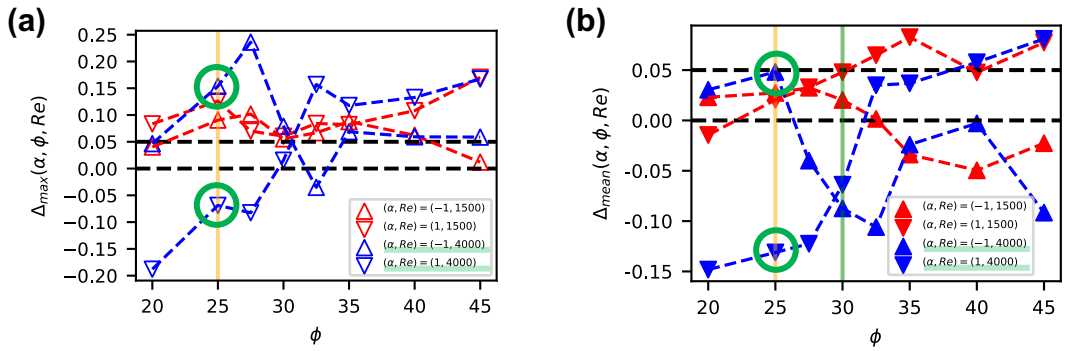

Figure 17: (a) $\Delta_{\max}(\alpha, \phi, Re)$ for $20^\circ \leq \phi \leq 45^\circ$. The triangle and inverted triangle indicate $\alpha = -1$ and $\alpha = 1$, respectively. Red and blue symbols indicate $Re = 1500$ and $Re = 4000$, respectively. (b) $\Delta_{\text{mean}}(\alpha, \phi, Re)$ for $20^\circ \leq \phi \leq 45^\circ$. Reprinted from Ref. [37].

This chapter aims to confirm the factors that enhance the performance of corrugated wings in comparison to the flat wing. It is demonstrated that wing performance is not solely determined by the AoA, wing shape, and Reynolds numbers. Fig. 17 (a) presents $\Delta_{\max}(\alpha, \phi, Re)$. Based on Figure 17 (a), it can be observed that $\Delta_{\max}(1, \phi, 4000)$ takes on negative values when ϕ is less than 30°. This indicates that the performance of the corrugated wing does not improve in this range. On the other hand, values of $\Delta_{\max}(1, \phi, 4000)$ become positive for $\phi \geq 30^\circ$, indicating an enhanced wing performance. This leads to the wing's transition occurring at $\phi \simeq 30^\circ$ (Fig. 6). Nevertheless, $\Delta_{\max}(-1, \phi, 4000)$ gives positive values for all ϕ calculated, except for the narrow range of $32^\circ \leq \phi \leq 34^\circ$, where slightly negative values are recorded (Fig. 6). With $Re = 1500$, the behavior of $\Delta_{\max}$ differs significantly; both $\Delta_{\max}(\pm 1, \phi, 1500)$ are positive, and no transition is observed.

Figure 17 (b) depicts $\Delta_{\text{mean}}(\alpha, \phi, Re)$. It is observed that $\Delta_{\text{mean}}(1, \phi, 4000)$ is negative for $\phi \leq 30^\circ$ and positive for $\phi > 30^\circ$. These findings parallel those of $\Delta_{\max}(1, \phi, 4000)$. However, it is essential to note that such consistency does not universally prevail.

Indeed, $\Delta_{\text{mean}}(-1, \phi, 4000)$ exhibits positive values for $\phi < 30^\circ$ and negative values for $\phi \geq 30^\circ$. Similarly, $\Delta_{\text{mean}}(-1, \phi, 1500)$ demonstrates positivity for $\phi \leq 30^\circ$ and negativity for $\phi > 30^\circ$ (Fig. 17 (b)). Consequently, the wing performance in these scenarios undergoes a transition around $\phi = 30^\circ$ (Fig. 17 (b); green line). It is noteworthy that the behaviors of $\Delta_{\max}(-1, \phi, 4000)$ and $\Delta_{\max}(-1, \phi, 1500)$ differ from those of $\Delta_{\text{mean}}(-1, \phi, 4000)$ and $\Delta_{\text{mean}}(-1, \phi, 1500)$, as previously discussed. Moreover, the transition point closely aligns with the case $(\alpha, Re) = (1, 4000)$, albeit with an opposite sign in Δ_{mean}.

4.3.2 Vorticity field around wings in the case $\phi = 25^\circ$

The correlation between wing performance and the vortex dynamics surrounding the wings is shown by examining the case with $\phi = 25^\circ$ and $Re = 4000$ (Fig. 17; green lines in legend). Figures 18 (a-1), (a-2), and (a-3) depict the vorticity fields at a specific time $t^* = t_{\text{v}}^*$ when the characteristic vortex distribution becomes

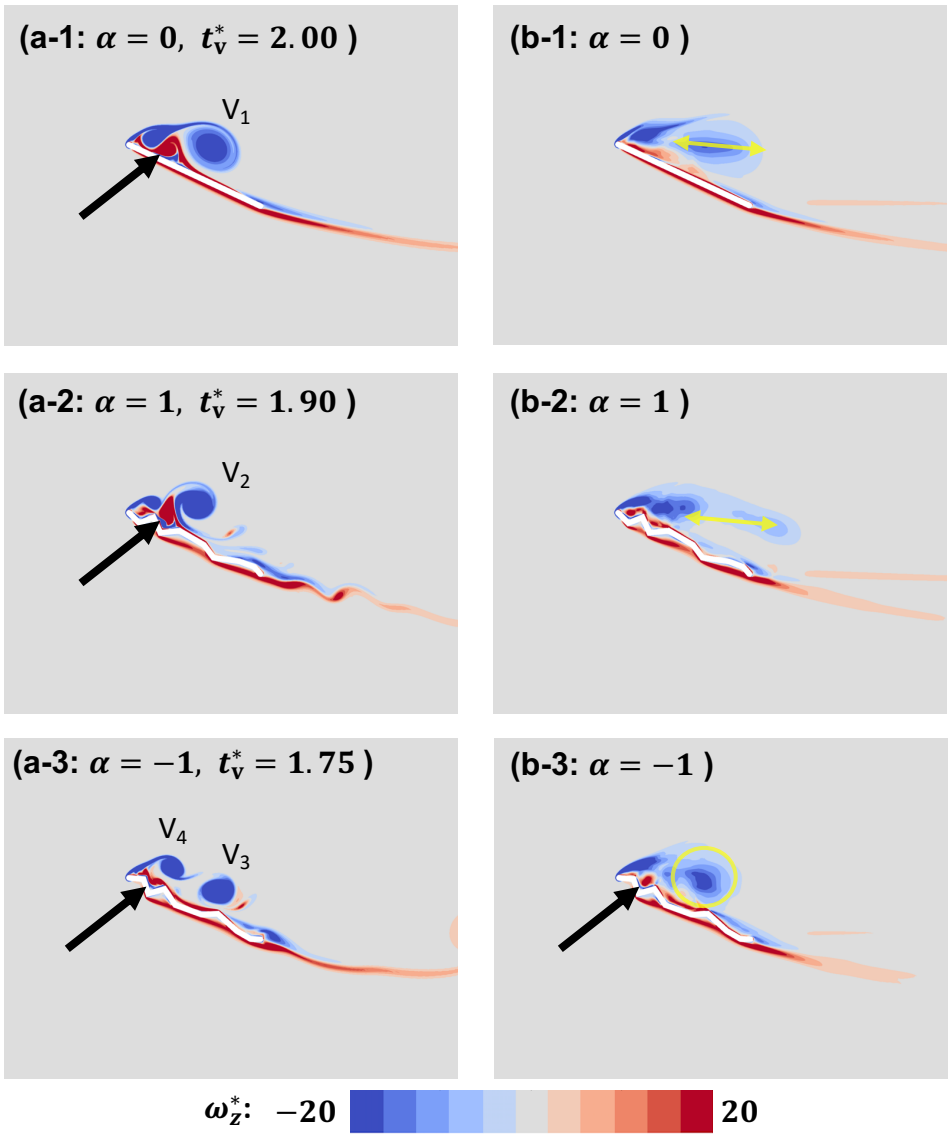

Figure 18: Vorticity fields for $\phi = 25°$ and $Re = 4000$. (a-1) Instantaneous field for the flat wing model ($\alpha = 0$) at $t_v^* = 2.00$. (a-2) Instantaneous field for the corrugated wing model ($\alpha = 1$) at $t_v^* = 1.90$. (a-3) Instantaneous field for the inverted corrugated wing model ($\alpha = -1$) at $t_v^* = 1.75$. (b-1) Mean field for the flat wing model ($\alpha = 0$). (b-2) Mean field for the corrugated wing model ($\alpha = 1$). (b-3) Mean field for the inverted corrugated wing model ($\alpha = -1$). Reprinted from Ref. [37].

evident. It is important to note that $t^*_{\mathrm{max}} \neq t^*_{\mathrm{v}}$. Furthermore, the mean vorticity fields are illustrated in Figs. 18 (b-1), (b-2), and (b-3).

In the scenario depicted in Fig. 18 (a-2); $\alpha = 1$, the lambda vortex is positioned between two LEVs, as indicated by the arrow, mirroring the arrangement observed in the case of the flat wing ($\alpha = 0$). Both in the corrugated wing ($\alpha = 1$) and the case of the flat wing ($\alpha = 0$), the LEVs V_1 and V_2, located closer to the trailing edge, moved away from the wing due to the influence of the lambda vortex. As a result, the mean vorticity field exhibited an elongated region with a negative sign in an oblique direction to the wing (Figs. 18 (b-1) and (b-2); indicated by yellow arrows). Consequently, the mean vorticity field exhibits a similarity to that observed in the flat wing case. This is a similar result to the $\alpha = 1, \phi = 20^\circ$ in the Chapter 3.

Figure 18 (a-3) presents the vorticity field surrounding the inverted corrugated wing ($\alpha = -1$). At $t^* = t^*_{\mathrm{v}}$, two vortices with a negative sign are evident above the wing, but the lambda vortex loses its characteristic shape (Figs. 18 (a-3) and (b-3); indicated by arrows). This is a similar result to the $\alpha = 1, \phi = 35^\circ$ in the Chapter 3.

These qualitative features were also observed in the case of $Re = 1500$ (data not shown). These results are comparable to the results presented in Chapter 3. Thus, the correlation between vortex motion and the enhancement of aerodynamic performance in the corrugated wing is independent of both the Reynolds number and model geometry.

4.4 Summary

This chapter examined two types of corrugated wing models at two Reynolds number cases, $Re = 1500$ or 4000. When the maximum coefficient of lift ($C_{L,\mathrm{max}}$) for the corrugated wing exceeded that of the flat wing, the collapse of the lambda vortex occurred on the corrugated structure. Consequently, split LEVs primarily interacted among themselves, akin to the observations in Chapter 3. This vortex motion was observed to enhance lift, irrespective of the specific corrugated structures and Reynolds numbers investigated.

Chapter 5

Concluding remarks

5.1 Summary

This study focused on the uneven structure in corrugated wings and analyzed flow patterns obtained by direct numerical simulation.

The analysis initially included a flow analysis around a triangular model with a bottom surface as the simplest example of a corrugated structure (Chapter 2). An increase in the Reynolds number resulted in a noticeable change in flow dynamics, especially at $Re = O(10^3)$. This led to a more pronounced manifestation of vortex structures. The flow transition was also observed as the two models moved closer together and became more complex uneven structures. These characteristics indicate that the flow around the corrugated wing is dynamic and that it can affect the aerodynamic performance.

A flow analysis was conducted to compare the performance of a two-dimensional corrugated wing with that of a flat wing at $Re = 4000$ (Chapter 3). The corrugated wing ($\alpha = 1$; α defines the shape of the corrugated wing) exhibited superior aerodynamic performance to the flat wing at an AoA of $\phi > 30°$. The lambda vortex collapsed on the corrugated wing, and the split LEV interacted with it, resulting in increased lift. The relationship between the collapse of the lambda vortex and increased lift is supported by quantitative indices.

The collapse of the lambda vortex has also been observed in the corrugated wing models with inverted shape ($\alpha = -1$) and at other Reynolds numbers ($Re = 1500$), indicating a lift enhancement mechanism (Chapter 4). The relationship by quantitative indices has been considered for other Reynolds numbers, with generally consistent results (data not shown). Further details will be reported elsewhere.

5.2 Discussions

The relationship between lambda vortex motion and lift enhancement revealed in this study provides a basis for future analysis of corrugated wings. This study has delineated certain characteristic dynamics associated with lift enhancement in the corrugated wing, relying on a simplified model of the wing and its motion. This approach stems from the complexity inherent in both the wing-shape details and vortex motion in the realistic scenario of a flapping dragonfly's wing. These simplifications intentionally omit details related to three-dimensionality and intricate flapping motion. However, the suggested dynamics will be beneficial for tackling more realistic models of a dragonfly's corrugated wing. This is because these simplifications are

based on fundamental dynamics associated with the LEV and uneven structures.

To better relate the present results to the flapping flight of insects, the potential for real-life dragonflies to collapse lambda vortices should be considered. Previous research has suggested a correlation between the static properties of corrugated wings and the confinement of vortices to a V-shaped region [2, 21, 28, 30, 33, 34]. Dragonfly wings contain neural pathways that are predominantly concentrated along the leading edge, suggesting an ability to perceive flow information [53]. One possibility is that the undulating structure of dragonfly wings may have a function in confining vortices within the indentations. In essence, dragonflies may be able to fly by collapsing lambda vortex with their flapping motion. Furthermore, in future evolutionary processes, dragonfly wings may undergo structural changes to more effectively disrupt lambda vortices.

Mechanisms described in this study hold promise for innovative wing-shape designs, especially in the low-Reynolds-number regime associated with insect flight. This parallels the concept of passive drag reduction in turbulent flow, where drag reduction of around 8% can be achieved by altering the surface shape [3, 54]. However, it is imperative to account for the influence of other parameters, such as the size of the V-shaped structure. In practice, Chapter 4 examined the performance of two types of corrugated wing models. The signs of the relative difference in $C_{L,\max}$ between the corrugated wing ($\alpha = 1$) and the flat wing ($\alpha = 0$), $\Delta_{\max}(1, \phi, Re)$, were negative for $\phi < 30°$ and $Re = 4000$ (Fig. 17 (a)). On the other hand, the signs of $\Delta_{\max}(-1, \phi, Re)$ were positive for most of the ϕ and Reynolds number investigated (Fig. 17 (a)). Therefore, it is anticipated that the structural details of the model with $\alpha = -1$ exhibit favorable characteristics for entrapping the lambda vortices. While the corrugated wing model with $\alpha = -1$ is an inversion of the wing model with $\alpha = 1$, a notable difference lies in the number of V-shaped structures (concavity at the upper side of the wing) in the model (Figs. 16 (b) and (c)). In the that cases with a negative sign of $\Delta_{\max}(1, \phi, Re)$ correspond to the eruption of the lambda vortex, consistently observed in the second V-shaped structure counted from the leading edge, the presence of only one V-shaped structure may hold significance for the overall vortex entrapment characteristics. The second V-shaped structure might facilitate the eruption of the lambda vortex. In light of the explored parameters, a single V-shaped structure appears to be more effective in suppressing the eruption of the lambda vortex. A more comprehensive characterization of the corrugated wing can be achieved by observing the presented scenario under more different parameters, which will be detailed in future works.

There were also new approaches in this analysis. This study focused on the spatiotemporal distribution of vorticity and pressure in a specific region above the corrugated wing, establishing a correlation between flow structures and the mechanism of lift enhancement (Chapter 3). This approach represents a novel method for analyzing the flow around the corrugated wing. Traditionally, attention is given to the spatiotemporal distribution of vorticity and pressure on the wing surface in the case of the flat wing [36]. However, to account for the intricate structure of corrugated wings, it was necessary to select a region slightly away from the wing surface. The results of this study indicate that it is not strictly necessary to focus solely on the wing surface when correlating flow structures around the wing with the lift enhancement mechanism. This suggests the potential for facilitating the analysis of the corrugated wing with complex structures. Further detailed investigations on this aspect will be essential in future research.

5.3 Perspectives

The question of whether dragonflies actually manipulate flow is intriguing. This study has focused on evaluating the dynamic characteristics, extracting a portion of the flapping motion, though not precisely copying the real flapping motion. Flapping motions involve various elements, including translational and rotational movements. It is interesting to investigate if significant vortex dynamics occur in these motions.

And, it is important to examine whether the results obtained in this study are observable on wings replicating the flapping motion. Similarly, understanding the wing movements required to induce the observed vortex dynamics in this study is crucial. These investigations not only help us to understand insect flapping flight but also pave the way for creating flapping robots that surpass insects in performance.

The results of the present study (especially in Chapter 3) need to be examined in a wider parameter range. The significance of Reynolds number dependency cannot be overstated. The qualitative trends have been consistently validated at Reynolds numbers of $Re = 1500$ and 4000 (Chapter 4). However, at $Re = 1500$, incomplete collapses of the lambda vortex were noted, characterized by less pronounced structural changes in coherent vortices compared to the cases at $Re = 4000$. This suggests that, at lower Reynolds numbers, viscous effects might cause deviations in the vortex dynamics from the illustrated scenario. Future works should provide a more comprehensive discussion of these observations.

This investigation utilized two-dimensional models. However, in the case of the three-dimensional nature of insect flight aerodynamics, the applicability of these findings extends to such scenarios. Extrapolating these results to a three-dimensional system holds the promise of yielding more practical insights into comprehending insect flights and their potential industrial applications. The investigation of three-dimensional space will be a central focus of my future research. Additionally, delving into the actual flapping motion would contribute to a more nuanced understanding of corrugated wings.

Acknowledgments

I am grateful to my supervisor Prof. Makoto Iima (Hiroshima University) for their polite guidance and help in research and writing papers. In Chapter 2, I am grateful to Prof. Hiraku Nishimori (Meiji University) for fruitful discussions from planning to publish this research [45]. I thank Prof. Satoshi Nakata and Prof. Koichi Fujimoto for the useful discussion. I would like to take this opportunity to thank you.

This work was supported by JSPS KAKENHI (19K03671, 21H05303, 22KJ2316) and the SECOM Science and Research Foundation.

Also, I give all of the members of the Laboratory of Fluid Mathematics for Life (Hiroshima University) my gratitude.

Reference

[1] Andrei K Brodsky. The evolution of insect flight. Oxford University Press, 1994.

[2] Richard J Bomphrey, Toshiyuki Nakata, Per Henningsson, and Huai-Ti Lin. Flight of the dragonflies and damselflies. Philosophical Transactions of the Royal Society B: Biological Sciences, 371(1704):20150389, 2016.

[3] Yusuke Fujita and Makoto Iima. Dynamic lift enhancement mechanism of dragonfly wing model by vortex-corrugation interaction. Physical Review Fluids, 8:123101, Dec 2023.

[4] Jeff D Eldredge and Anya R Jones. Leading-edge vortices: mechanics and modeling. Annual Review of Fluid Mechanics, 51:75–104, 2019.

[5] Loan Thi Kim Au, Hoang Vu Phan, Soo Hyung Park, and Hoon Cheol Park. Effect of corrugation on the aerodynamic performance of three-dimensional flapping wings. Aerospace Science and Technology, 105:106041, 2020.

[6] Javaan Chahl, Nasim Chitsaz, Blake McIvor, Titilayo Ogunwa, Jia-Ming Kok, Timothy McIntyre, and Ermira Abdullah. Biomimetic drones inspired by dragonflies will require a systems based approach and insights from biology. Drones, 5(2):24, 2021.

[7] John Holbert, Amal Jacob, Nick Peters, and Zack Sternberg. Vertical axis windmill. American Journal of Mechanical Engineering, 6(1):1–5, 2018.

[8] Akira Obata, Shotarou Shinohara, Kyohei Akimoto, Kakeru Suzuki, and Miyuki Seki. Aerodynamic bio-mimetics of gliding dragonflies for ultra-light flying robot. Robotics, 3(2):163–180, 2014.

[9] Chenyang Wang, Weiping Zhang, Yang Zou, Ran Meng, Jiaxin Zhao, and Mingchen Wei. A sub-100 mg electromagnetically driven insect-inspired flapping-wing micro robot capable of liftoff and control torques modulation. Journal of Bionic Engineering, 17:1085–1095, 2020.

[10] Charles P Ellington, Coen Van Den Berg, Alexander P Willmott, and Adrian LR Thomas. Leading-edge vortices in insect flight. Nature, 384(6610):626–630, 1996.

[11] Charles Porter Ellington. The aerodynamics of hovering insect flight. iv. aerodynamic mechanisms. Philosophical Transactions of the Royal Society of London. B, Biological Sciences, 305(1122):79–113, 1984.

[12] Diana D Chin and David Lentink. Flapping wing aerodynamics: from insects to vertebrates. Journal of Experimental Biology, 219(7):920–932, 2016.

[13] Michael H Dickinson and Karl G Götz. Unsteady aerodynamic performance of model wings at low Reynolds numbers. Journal of experimental biology, 174(1):45–64, 1993.

[14] Sanjay P Sane. The aerodynamics of insect flight. Journal of experimental biology, 206(23):4191–4208, 2003.

[15] Wei Shyy, Chang-kwon Kang, Pakpong Chirarattananon, Sridhar Ravi, and Hao Liu. Aerodynamics, sensing and control of insect-scale flapping-wing flight. Proceedings of the Royal Society A: Mathematical, Physical and Engineering Sciences, 472(2186):20150712, 2016.

[16] Michael H Dickinson, Fritz-Olaf Lehmann, and Sanjay P Sane. Wing rotation and the aerodynamic basis of insect flight. Science, 284(5422):1954–1960, 1999.

[17] Torkel Weis-Fogh. Quick estimates of flight fitness in hovering animals, including novel mechanisms for lift production. Journal of experimental Biology, 59(1):169–230, 1973.

[18] Robert Dudley. The biomechanics of insect flight: form, function, evolution. Princeton University Press, 2002.

[19] DJS Newman and RJ Wootton. An approach to the mechanics of pleating in dragonfly wings. Journal of Experimental Biology, 125(1):361–372, 1986.

[20] Hamed Rajabi, M Rezasefat, A Darvizeh, J-H Dirks, SH Eshghi, A Shafiei, T Mirzababaie Mostofi, and Stas N Gorb. A comparative study of the effects of constructional elements on the mechanical behaviour of dragonfly wings. Applied Physics A, 122:1–13, 2016.

[21] Mohd Imran Ansari, Mohammed Hamid Siddique, Abdus Samad, and Syed Fahad Anwer. On the optimal morphology and performance of a modeled dragonfly airfoil in gliding mode. Physics of Fluids, 31(5):051904, 2019.

[22] Syed Fahad Anwer, Intesaaf Ashraf, Husain Mehdi, Akhlaq Ahmad, and H Grafi. On the aerodynamic performance of dragonfly wing section in gliding mode. Advances in Aerospace Science and Applications, 3:227–234, 2013.

[23] RH Buckholz. The functional role of wing corrugations in living systems. Journal of Fluids Engineering, 108(1):93–97, 1986.

[24] Hui Hu and Masatoshi Tamai. Bioinspired corrugated airfoil at low —Reynolds numbers. Journal of Aircraft, 45(6):2068–2077, 2008.

[25] David-Elie Levy and Avraham Seifert. Simplified dragonfly airfoil aerodynamics at Reynolds numbers below 8000. Physics of fluids, 21(7):071901, 2009.

[26] David-Elie Levy and Avraham Seifert. Parameter study of simplified dragonfly airfoil geometry at Reynolds number of 6000. Journal of theoretical biology, 266(4):691–702, 2010.

[27] Xue Guang Meng and Mao Sun. Aerodynamic effects of wing corrugation at gliding flight at low Reynolds numbers. Physics of Fluids, 25(7):071905, 2013.

[28] Abel Vargas, Rajat Mittal, and Haibo Dong. A computational study of the aerodynamic performance of a dragonfly wing section in gliding flight. Bioinspiration & biomimetics, 3(2):026004, 2008.

[29] Zilong Zhang, Yajun Yin, Zheng Zhong, and Hongxiao Zhao. Aerodynamic performance of dragonfly wing with well-designed corrugated section in gliding flight. Computer Modeling in Engineering & Sciences, 109(3):285–302, 2015.

[30] BG Newman, SG Savage, and D Schouella. Model tests on a wing section of an aeschna dragonfly. scale effects in animal locomotion (1977) edited by pedley, tj, 1977.

[31] JM Wakeling. Dragonfly aerodynamics and unsteady mechanisms: a review. Odonatologica, 22(3):319–334, 1993.

[32] Antonia B Kesel. Aerodynamic characteristics of dragonfly wing sections compared with technical aerofoils. Journal of experimental biology, 203(20):3125–3135, 2000.

[33] A Obata and S Sinohara. Flow visualization study of the aerodynamics of modeled dragonfly wings. AIAA journal, 47(12):3043–3046, 2009.

[34] Christopher JC Rees. Aerodynamic properties of an insect wing section and a smooth aerofoil compared. Nature, 258(5531):141–142, 1975.

[35] Yeon Sik Baik, Luis P Bernal, Kenneth Granlund, and Michael V Ol. Unsteady force generation and vortex dynamics of pitching and plunging aerofoils. Journal of Fluid Mechanics, 709:37–68, 2012.

[36] David E Rival, Jochen Kriegseis, Pascal Schaub, Alexander Widmann, and Cameron Tropea. Characteristic length scales for vortex detachment on plunging profiles with varying leading-edge geometry. Experiments in fluids, 55:1–8, 2014.

[37] Yusuke Fujita and Makoto Iima. Aerodynamic performance of dragonfly wing model that starts impulsively: how vortex motion works. Journal of Fluid Science and Technology, 18(1):JFST0013–JFST0013, 2023.

[38] A Widmann and C Tropea. Parameters influencing vortex growth and detachment on unsteady aerodynamic profiles. Journal of Fluid Mechanics, 773:432–459, 2015.

[39] Guoyu Luo and Mao Sun. The effects of corrugation and wing planform on the aerodynamic force production of sweeping model insect wings. Acta Mechanica Sinica, 21(6):531–541, 2005.

[40] G Rüppell. Kinematic analysis of symmetrical flight manoeuvres of odonata. Journal of experimental Biology, 144(1):13–42, 1989.

[41] Z Jane Wang. The role of drag in insect hovering. Journal of Experimental Biology, 207(23):4147–4155, 2004.

[42] Thierry Jardin, Jeesoon Choi, and Tim Colonius. An empirical correlation between lift and the properties of leading-edge vortices. Theoretical and Computational Fluid Dynamics, 35(4):437–448, 2021.

[43] Daegyoum Kim and Morteza Gharib. Flexibility effects on vortex formation of translating plates. Journal of fluid mechanics, 677:255–271, 2011.

[44] Matthew J Ringuette, Michele Milano, and Morteza Gharib. Role of the tip vortex in the force generation of low-aspect-ratio normal flat plates. Journal of Fluid Mechanics, 581:453–468, 2007.

[45] Yusuke Fujita, Hiraku Nishimori, and Makoto Iima. Dead-water region around two-dimensional sand-dune models. Journal of the Physical Society of Japan, 89(6):063901, 2020.

[46] Feng Bao and Uwe Ch Dallmann. Some physical aspects of separation bubble on a rounded backward-facing step. Aerospace Science and Technology, 8(2):83–91, 2004.

[47] DK Heist and FC Gouldin. Turbulent flow normal to a triangular cylinder. Journal of Fluid Mechanics, 331:107–125, 1997.

[48] D Sumner. Two circular cylinders in cross-flow: A review. Journal of fluids and structures, 26(6):849–899, 2010.

[49] Anthony T Patera. A spectral element method for fluid dynamics: laminar flow in a channel expansion. Journal of computational Physics, 54(3):468–488, 1984.

[50] George Em Karniadakis, George Karniadakis, and Spencer Sherwin. Spectral/hp element methods for computational fluid dynamics. Oxford University Press on Demand, 2005.

[51] Hugh M Blackburn, D Lee, Thomas Albrecht, and Jagmohan Singh. Semtex: a spectral element–fourier solver for the incompressible navier–stokes equations in cylindrical or cartesian coordinates. Computer Physics Communications, 245:106804, 2019.

[52] Suchuan Dong, George E Karniadakis, and Chryssostomos Chryssostomidis. A robust and accurate outflow boundary condition for incompressible flow simulations on severely-truncated unbounded domains. Journal of Computational Physics, 261:83–105, 2014.

[53] Joseph Fabian, Igor Siwanowicz, Myriam Uhrhan, Masateru Maeda, Richard J Bomphrey, and Huai-Ti Lin. Systematic characterization of wing mechanosensors that monitor airflow and wing deformations. Iscience, 25(4):104150, 2022.

[54] Brian Dean and Bharat Bhushan. Shark-skin surfaces for fluid-drag reduction in turbulent flow: a review. Philosophical Transactions of the Royal Society A: Mathematical, Physical and Engineering Sciences, 368(1929):4775–4806, 2010.